V_S and density structure beneath the Colorado Plateau constrained by gravity anomalies and joint inversions of receiver function and phase velocity data

Iain W. Bailey,[1] Meghan S. Miller,[1] Kaijian Liu,[2,3] and Alan Levander[2]

Received 12 May 2011; revised 22 December 2011; accepted 28 December 2011; published 25 February 2012.

[1] The Colorado Plateau is a physiographic province in the western US with an average elevation of ~1.9 km where, in contrast to neighboring provinces, there is little evidence of large scale tectonic deformation or magmatism. Recent availability of Earthscope/USArray seismic data allow us to better examine the crust and upper mantle structure beneath the region and test proposed explanations for the plateau's uplift and relative stability. Using phase velocities for fundamental mode Rayleigh waves and P receiver functions, we perform over 800 joint inversions for 1-D shear wave velocity V_S profiles sampling the plateau and surrounding regions down to 150 km depth. We image a sharp change in crustal thickness at the western edge of the Colorado Plateau with a more gradual increase eastward moving into the Rocky Mountains. A relatively thick (≳100 km) lithosphere beneath the plateau extends into the Rocky Mountains to the north. We use empirical scaling relations to estimate densities from our V_S results, and predict the associated gravity anomalies, which are inconsistent with the observed distribution of the Bouguer gravity anomalies. We somewhat reconcile the prediction and observations by assuming that lateral density variations below 50 km can be ignored and the lithospheric root is therefore neutrally buoyant. While there is some evidence for small scale convection and lithospheric removal at its edges, the shape of the lithospheric mantle anomaly is consistent with a large scale uplift of the plateau by heating since removal of the Farallon slab. We conclude that the lithospheric root is key to the long term stability of the Colorado Plateau, leading to a colder, stronger crust.

Citation: Bailey, I. W., M. S. Miller, K. Liu, and A. Levander (2012), V_S and density structure beneath the Colorado Plateau constrained by gravity anomalies and joint inversions of receiver function and phase velocity data, *J. Geophys. Res.*, *117*, B02313, doi:10.1029/2011JB008522.

1. Introduction

[2] The Colorado Plateau (CP) has been a subject of scientific interest since early geological exploration of the Western US in the nineteenth century [e.g., *Gilbert*, 1875; *Dutton*, 1880]. It remains a topic of discussion since ~90% of its area has an elevation above 1.5 km, despite little evidence of compressional/extensional tectonics or widespread magmatism. This contrasts with the neighboring Rocky Mountains (RM) dominated by compressional tectonic features, and Northern Basin and Range (NBR), Arizona Transition Zone (ATZ) and Rio Grande Rift (RGR) dominated by extensional tectonic features (Figure 1). Widespread Upper Cretaceous marine sediments show that the plateau was at sea level ~80 Ma [*Flowers et al.*, 2008], and a number of explanations have been proposed for how and when subsequent uplift has occurred. Nearly all explanations are placed in the context of the Laramide orogeny that involved low angle subduction of the Farallon slab beneath the Western US from ~90 Ma, generating widespread volcanism that progressed eastward over time. A subsequent onset of volcanism in the NBR and Southern Basin and Range (SBR) known as the ignimbrite flare-up progressed synchronously from the south and from the north around 54–21 Ma. This is often associated with break off of the slab [*Humphreys*, 1995]. During and subsequent to the ignimbrite flare-up, there have been periods of extension in provinces to the west, south and southeast of the plateau that were notably active 35–20 Ma in the RGR [*Morgan et al.*, 1986], 25–15 Ma in the ATZ and SBR [*Spencer et al.*, 1995].

[3] Paleoelevation data for the CP tend to suggest spatially non-uniform uplift that was mostly coeval to the Laramide orogeny [e.g., *Wolfe et al.*, 1998; *Flowers et al.*, 2008; *Huntington et al.*, 2010] though some results suggest later uplift [e.g., *Sahagian et al.*, 2002; *Karlstrom et al.*, 2008]. *Liu and Gurnis* [2010] showed that dynamic uplift

[1]Department of Earth Sciences, University of Southern California, Los Angeles, California, USA.
[2]Department of Earth Sciences, Rice University, Houston, Texas, USA.
[3]Applied Physics Program, Rice University, Houston, Texas, USA.

0148-0227/12/2011JB008522

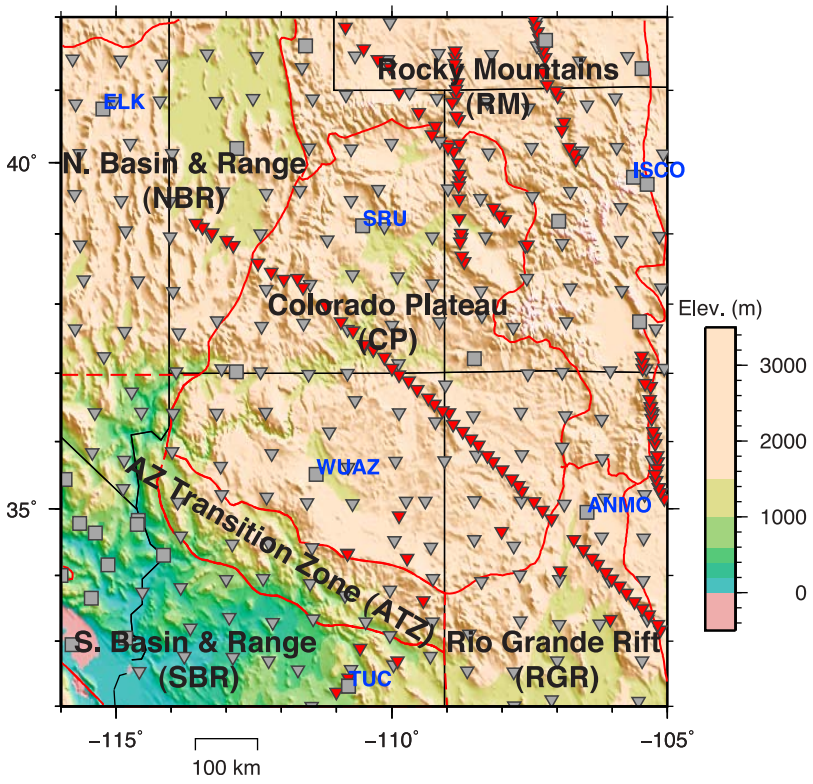

Figure 1. Topographic map of the Colorado Plateau and surrounding tectonic provinces. Red lines delineate boundaries of the tectonic provinces and black lines show state boundaries. Gray squares show the locations of permanent and semi-permanent stations, gray triangles show the locations of TA stations, and red triangles show the locations of temporary stations. Blue text marks the names and locations of permanent stations used in subsequent example inversions.

associated with shallow slab subduction can explain the paleoelevation data of *Flowers et al.* [2008], with additional uplift and support of the elevations by a deep mantle upwelling. However, the average free air anomaly for the plateau is close to zero, indicating isostatic equilibrium [*Thompson and Zoback*, 1979], and many authors focus on buoyancy of the crust and/or mantle lithosphere to explain support and uplift of the plateau.

[4] Observations based on teleseismic data show thick (∼45 km) crust [e.g., *Zandt et al.*, 1995; *Lastowka et al.*, 2001; *Wilson et al.*, 2010] that cannot be explained by Laramide shortening estimates of <1% [*Spencer*, 1996]. Controlled source refraction seismic methods provide more accurate, yet localized measurements of crustal thickness. Results from the PACE experiment suggest a ∼40–48 km crustal thickness beneath the Four Corners region and the southwest CP compared to ∼35 km thickness beneath the SBR [*Wolf and Cipar*, 1993; *Parsons et al.*, 1996]. Results from the Deep Probe experiment profiling the 108°W meridian [*Henstock et al.*, 1998; *Snelson et al.*, 1998; *Gorman et al.*, 2002] show a non-uniform crustal thickness of ∼40 km beneath the northern CP boundary and ∼35 km at the southern edge of the CP. Various mechanisms have been proposed for crustal thickening during or subsequent to the Laramide orogeny [*Bird*, 1984; *Morgan and Swanberg*, 1985; *McQuarrie and Chase*, 2000]. However, the observed crustal thickness still requires above average buoyancy of the underlying mantle for isostatic balance [*Lastowka et al.*, 2001]. Hence, although there is strong evidence for a CP crust that is somehow distinct from surrounding regions, additional mechanisms are required for uplift and support of the elevations.

[5] Suggestions for low mantle density include various mechanisms for removal of the lithosphere replaced by hot and buoyant asthenosphere [*Bird*, 1988; *Beghoul and Barazangi*, 1989; *Spencer*, 1996; *van Wijk et al.*, 2010], buoyancy modification by hydration of the lithosphere [*Humphreys et al.*, 2003], and differential heating of a pervasively thick and depleted lithosphere [*Roy et al.*, 2009]. Interpretation of seismic data from the LaRiSTra profile, which crossed the NBR, CP and RGR in a northwest–southeast direction, shows low velocity mantle beneath the NBR and RGR [*West et al.*, 2004; *Sine et al.*, 2008; *Wilson et al.*, 2010]. This indicates that some of the lithosphere has been removed in those provinces, but a sharp increase in mantle velocities at the NBR/CP boundary indicates that the lithosphere is thicker beneath the CP. Hence, there is little evidence for CP uplift mechanisms that require significant widespread removal of the lithosphere [e.g., *Morgan and Swanberg*, 1985; *Bird*, 1988]. However, there is evidence of localized removal of lithosphere at the edges of the CP [e.g., *Levander et al.*, 2011], and modeling by *van Wijk et al.* [2010] shows that small-scale convection beneath the CP boundaries can be a factor in the support of high topography.

[6] In relation to the long term tectonic stability of the CP, flexural rigidity studies [e.g., *Lowry and Smith*, 1995]

indicate greater strength of the CP relative to the NBR. *Zandt et al.* [1995] suggested a strong mafic lower crust based on receiver functions that indicate higher V_P/V_S ratios in the west of the CP than in the east of the NBR. *Moschetti et al.* [2010] found higher crustal velocities for the CP from ambient noise tomography which they also interpreted as evidence for a more mafic crust. However, V_P/V_S computed by *Wilson et al.* [2010] for the LaRiSTra profile is quite variable within the CP suggesting that it is not underlain by uniform crustal properties. Although high lower crustal V_P values were found in the southwest CP from the PACE experiment [*Wolf and Cipar*, 1993], the Deep Probe experiment did not find high V_P in the lower crust beneath the southeast and east of the CP [*Snelson et al.*, 1998]. Furthermore, none of these studies extend to the northeastern boundary of the CP and examine the potential differences in crustal strength between the CP and RM.

[7] Nearly all previous seismic studies have focused on 2-D profiles [e.g., *Zandt et al.*, 1995; *West et al.*, 2004; *Sine et al.*, 2008; *Wilson et al.*, 2010] or sub-regions [e.g., *Lastowka et al.*, 2001; *Frassetto et al.*, 2006] around the boundaries of the CP then extrapolated to make interpretations for the entire plateau. Recent availability of USArray data allow detailed study of the entire region incorporating province boundaries and beyond. *Liu et al.* [2011] used these data to compute a 3-D V_S model for the region using a two stage inversion via computation of Rayleigh wave phase velocities. To constrain crustal thickness, they incorporated independent information from receiver functions. Here, we combine the same phase velocity results with receiver functions in joint inversions to compute a V_S model consistent with both data sets. Joint inversion of surface wave phase velocities and receiver function data sets has been shown previously to better image absolute velocities, using surface wave information, and sharp velocity discontinuities, using the receiver function information[*Julià et al.*, 2000]. The method has been used to image structure beneath the Arabian Shield [*Julià et al.*, 2003], Korean peninsula [*Yoo et al.*, 2007], and Cameroon [*Tokam et al.*, 2010]. We extend this to a larger region and data set than those studies, including over 8,000 receiver functions. The method is limited to inversion for 1-D V_S profiles, and by extracting common features of nearby results we generate a 3-D image of the subsurface V_S structure down to 150 km depth. The better resolution of the Moho and other discontinuities makes the V_S results well suited for comparison with gravity anomaly data. Several of the previous seismic studies have considered their results in terms of implications for density and isostatic balance [e.g., *Lastowka et al.*, 2001; *Wilson et al.*, 2010], though not comparing their results to gravity anomaly observations. *Roy et al.* [2005] used seismic models and geological data to help constrain lateral changes in density that predict Bouguer gravity anomalies in transects across the RGR and southeast CP. In this study we quantitatively compare Bouguer anomalies predicted from our seismic results to those computed from observed gravity anomalies across the entire region, and use the results to better understand density of the crust, lithospheric mantle and upper asthenosphere below the plateau and surrounding regions. Since the average free air anomaly is fairly small for the CP the density structure causing the Bouguer anomaly should explain much of the support for the region.

[8] The results support previous findings of a relatively thick crust with relatively high V_S beneath the CP, but also provide improved resolution of the entire plateau boundary. A sharp change in the Moho depth on the western, southern and southeastern boundaries is likely to be related to extension in those neighboring provinces. However, the transition of crustal thickness at the northeastern boundary with the compressional RM is more gradual. We also find a relative increase in lithospheric thickness based on a high velocity anomaly beneath the CP relative to the east, west and south. We discuss the possible origin of this lithosphere and its implications for the long term stability of the plateau. Our gravity analysis indicates that variations in the properties of the deeper (>50 km) mantle lithosphere appear to exert little effect on the observed Bouguer anomalies, indicating that the lithospheric root beneath the CP is neutrally buoyant with respect to the surrounding asthenosphere.

2. Data and Processing

2.1. Rayleigh Wave Phase Velocities

[9] The fundamental mode Rayleigh wave phase velocities used in this study were computed by *Liu et al.* [2011] via inversion over a 0.5 × 0.5° grid covering the region 32–42°N and 105–116°W. Data were taken from USArray TA and reference array stations for 154 shallow focus earthquakes occurring between July, 2007 and September, 2009 with moment magnitude $M_W \geq 5.5$ and a roughly uniform azimuthal coverage. The inversion method uses a two plane wave approximation incorporating 2-D finite frequency kernels to model Rayleigh wave propagation, multipathing and scattering effects [*Forsyth and Li*, 2005; *Yang and Forsyth*, 2006]. The method and results are described in detail by *Liu et al.* [2011], and here we extract velocities for 17 periods (20, 22, 25, 27, 30, 34, 40, 45, 50, 59, 67, 77, 87, 100, 111, 125 and 143 s). Uncertainties in the phase velocities are quantified by the residual data fit for each period in each grid cell of the inversion. As a result of the inversion, lateral smoothing is built into our input data and this influences the horizontal resolution of our model, as discussed in section 6.

2.2. Receiver Functions

[10] We use the program Standing Order for Data (SOD v2.2.2) [*Owens et al.*, 2004] to download three component data around P-wave arrivals with signal-to-noise ratio ≥2 for broadband, high-gain stations in the Colorado Plateau region defined by the same latitude and longitude ranges used for phase velocities. This incorporates the USArray TA from 2004–2009 and reference array stations from 1995–2009 as well as those from five PASSCAL temporary deployments: Deep Probe [*Dueker and Yuan*, 2004], CD-ROM [*Karlstrom et al.*, 2005], LaRiSTra [*West et al.*, 2004], LaRiSTra extension [*Sine et al.*, 2008] and COARSE [*Frassetto et al.*, 2006]. Events are selected with a moment magnitude greater than 5.5, depth in the range $1 \leq z \leq 600$ km and source-receiver distance in the range $30 \leq \Delta \leq 95°$. Slowness and back azimuth values for each P-wave raypath are computed using the AK-135 [*Kennett et al.*, 1995] velocity model.

[11] The seismograms are processed to remove the mean and trend, then band-pass filtered using a third order Butterworth filter with corner frequencies 0.02 and 1.5 Hz.

P receiver functions are computed for the time range $-10 \leq t \leq 50$ s by deconvolving the vertical from the radial component using the iterative method of *Ligorria and Ammon* [1999] with a Gaussian filter width of 1.5 and up to 200 iterations. If the RMS misfit to the filtered radial component is greater than 20% of the total power we assume the deconvolution was not successful and throw out the receiver function. This results in a raw data set of 9,480 P receiver functions. We then apply the following criteria to remove those dominated by unwanted signals: First, the maximum amplitude of the receiver function is required to be within 1 s of $t = 0$ since we expect the direct P arrival to dominate the signal. Secondly, the signal-to-noise ratio is required to be greater than 10, calculated as the average power for $-5 \leq t < 15$ divided by the average power for $-10 \leq t < -5$. This is the reason we calculate the receiver functions for $t < 0$, where the signal should be zero. In addition, to avoid outliers influencing subsequent stacking, we compute the trace power for each receiver function and remove any traces where the power is less than 10% of the median Ω_{50} or greater than $\Omega_{75} + 3/2(\Omega_{75} - \Omega_{50})$, where Ω_{75} is the 75th percentile. Our final data set contains 8,323 receiver functions from 355 stations.

[12] Using the Tectonic North America (TNA) [*Grand and Helmberger*, 1984] V_S model with a constant V_P/V_S ratio of 1.8 to map possible Ps conversion times to depth, these data are summarized in Figure 2. The hit count map in Figure 2a highlights the good coverage of the region provided by the TA data and the benefit of incorporating the closely spaced LaRiSTra stations. We obtain a relatively large number of good quality receiver functions in the SBR region. Due to the distribution of earthquake locations at teleseismic distances from the region, most receiver functions sample in either a NW, SW or SE direction from the individual stations (Figure 2b) with little in between. The cross-sections in Figure 2c reproduce a number of results noted in previous studies: an apparently deeper Moho beneath the CP relative to the SBR, NBR, and RGR regions [e.g., *Zandt et al.*, 1995; *Wilson et al.*, 2010], a relatively low amplitude Moho signal beneath the CP [e.g., *Gilbert et al.*, 2007], and an apparent double Moho beneath the western-central part of the CP [*Levander et al.*, 2011].

2.3. Bouguer Gravity Anomalies

[13] We use the same longitude/latitude limits as for phase velocities to select gravity measurements from the Gravity and Magnetic Dataset Repository [*Keller et al.*, 2006] at the University of Texas at El Paso. From a total of over 290,000 measurements, we average the complete Bouguer gravity anomaly values over a 0.5° grid (Figure 9a) and estimate standard deviation for each grid cell based on the variation of results. The complete Bouguer gravity anomaly incorporates corrections for the Bouguer and terrain model effects, as described by *Hinze et al.* [2005], but here we refer to this as the observed Bouguer anomaly for simplicity.

3. Joint Inversion Methods

[14] Our main analysis centers around the joint inversion of P receiver functions and Rayleigh wave phase velocities for numerous 1-D V_S profiles across the region. As outlined by *Julià et al.* [2000], these two data sets are consistent in that both are dominantly sensitive to V_S structure in the top ~250 km of the Earth. Furthermore, they are complimentary in that receiver functions are well suited for constraining velocity contrasts and poorly suited for constraining absolute velocities [e.g., *Ammon et al.*, 1990], while the opposite is true for surface wave phase velocities. We follow the method of *Julià et al.* [2000] and use the codes from the Computational Programs in Seismology package (R. B. Herrmann and C. J. Ammon, Computer programs in seismology 3.30: Surface waves, receiver functions and crustal structure, 2002, available at www.eas.slu.edu/People/RBHerrmann/CPS330.html), used for this purpose previously by *Yoo et al.* [2007]. The linearized forward problem can be written as

$$\begin{pmatrix} \sqrt{p}\mathbf{G}^{PV} \\ \sqrt{1-p}\mathbf{G}^{RF} \end{pmatrix} \delta\mathbf{m} = \begin{pmatrix} \sqrt{p}\ \widehat{\delta\mathbf{d}}^{PV} \\ \sqrt{1-p}\ \widehat{\delta\mathbf{d}}^{RF} \end{pmatrix}, \tag{1}$$

where $\delta\mathbf{m}$, $= \mathbf{m} - \mathbf{m}_0$, and $\mathbf{m} = (m_1, m_2, .., m_M)^T$ contains the velocities of the V_S profile, parameterized into layers of constant thickness, that best improves upon the fit to data predicted by the previous model $\mathbf{m}_0$. The residual vectors are in component form given by

$$\widehat{\delta d}_i^{PV} = \frac{c(T_i) - c'(T_i)}{N^{PV}\sigma_i};\ \widehat{\delta d}_i^{RF} = \frac{r(t_i) - r'(t_i)}{N^{RF}\sigma_i}, \tag{2}$$

which denote the normalized differences between observed $c(T_i)$, $r(t_i)$ and predicted $c'(T_i)$, $r'(t_i)$ phase velocities and receiver function amplitudes at the period T_i and time t_i, respectively, where N^{RF} is the number of time samples in the receiver function, N^{PV} is the number of phase velocities, and σ_i denotes the estimated standard error for that particular datum. The matrices $\mathbf{G}^{PV}$ and $\mathbf{G}^{RF}$ denote partial derivatives relating changes in predicted data to changes in the layer values of V_S, which are also normalized by the number of data and data standard errors. Relative influence of the two data sets is controlled by the parameter p such that if $p = 1$ we consider only the phase velocity data and if $p = 0$ we consider only the receiver function data. We iteratively solve for $\mathbf{m}$, incorporating a smoothness constraint that minimizes the second differences of V_S with depth in $\mathbf{m}$ weighted by a damping parameter γ, as well as using a weighting matrix $\mathbf{W}$ to minimize changes from $\mathbf{m_0}$ at the bottom of the model where data provide fewer constraints. The predictions r', C' and their associated partial derivative matrices are computed with the assumptions that $\mathbf{m}$ can be accurately represented by a stack of flat layers within which properties (V_P, V_S, density ρ, and attenuation factors for compressional and shear motion Q_κ^{-1} and Q_μ^{-1}) are constant and isotropic. In addition to layer thicknesses, values of V_P/V_S, ρ/V_S, Q_κ^{-1} and Q_μ^{-1} are constant throughout the inversion iterations.

[15] The starting point for all inversions is the AK-135 model of *Kennett et al.* [1995] interpolated to 2 km thick layers over $0 \leq z \leq 250$ km. Following the method of *Yoo et al.* [2007] upper mantle velocities are projected upwards to prevent the initial Moho depth from influencing the final Moho depth. From this initial model we perform inversions of just the phase velocities at the 0.5° spacing of the input data, We perform 2 iterations using high damping ($\gamma = 10$)

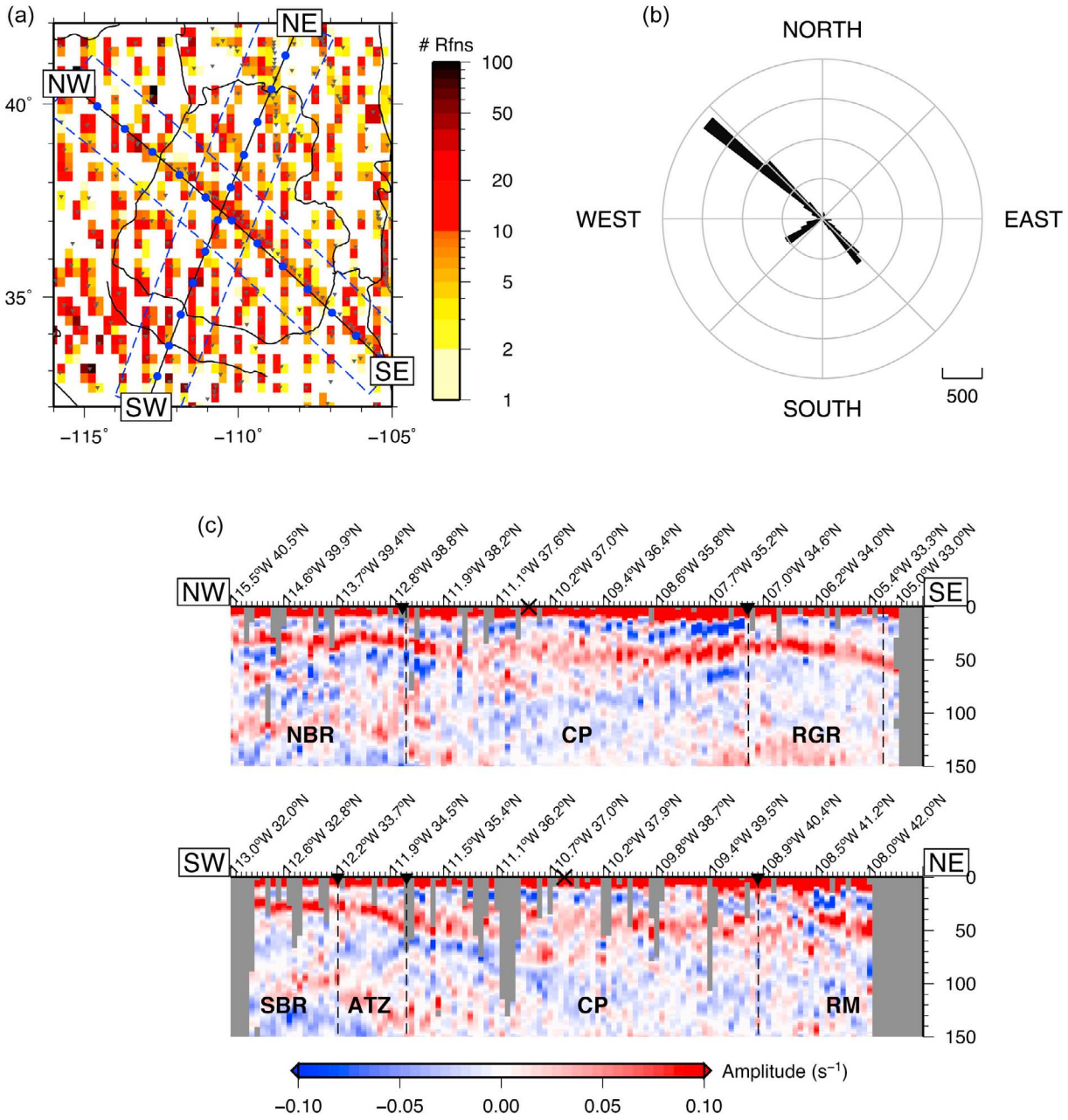

Figure 2. A summary of the 8,323 receiver functions computed in this study and mapped to depth using the TNA reference model. (a) Hit count for potential P to S conversion piercing points at z = 30 km on a 0.25° grid. Blue rectangles indicate the extent of data mapped to the cross sections, with blue circles denoting 100 km intervals along each profile. Gray triangles indicate the station locations. (b) Angular histogram of all receiver function back azimuths with a 5° bin width. (c) Common conversion point stacks of the receiver function amplitudes along the cross sections indicated in Figure 2a after mapping the P to S conversion path to depth with constant back azimuth and slowness. The stacks use a grid cell size of 2 km in depth, 10 km along the profile, and 200 km perpendicular to the profile. Plots show vertical exaggeration by a factor of two, while the color scale saturates at 0.1 s^{-1} to highlight coherent lateral signals. Black triangles and dashed lines show the tectonic province boundaries and black crosses at z = 0 show the point at which the profiles intersect.

followed by 30 iterations using γ = 0.1, chosen after assessment of roughness versus misfit trade-off curves for 20 randomly selected grid cells. Weighting is used in the lowest 50 km to obtain a smooth transition to the AK-135 model below 250 km. These inversions are less sensitive to the initial model than the joint inversion due to the broad, overlapping sensitivity kernels of the Rayleigh wave phase velocities. The results give a smoothly varying 3-D velocity

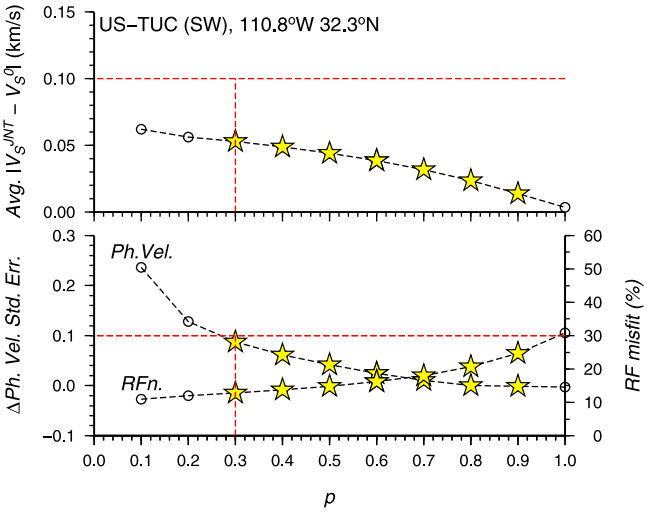

Figure 3. Using the SW gather at station US TUC as an example, data misfit and change in V_S model as a function of the joint inversion influence parameter p. Horizontal red dashed lines show the upper cutoff for accepting the inversion result and stars show all results that satisfy these conditions. The value of p chosen as the final result based on the minimum receiver function misfit is indicated by a vertical red dashed line.

model similar to *Liu et al.* [2011] providing constraints on the absolute V_S structure which we use for the initial models in the joint inversions.

[16] We apply the joint inversion method to our data by computing up to four separate inversions for each station after grouping receiver functions from NE, SE, SW and NW arrivals. This separation by back-azimuth is suitable given the dominant arrival directions in the data (Figure 2b) and allows us to reduce the bias toward a NW-SE sampling of the lithosphere and upper mantle. In addition, we can assess the suitability of a 1-D velocity structure beneath each station by comparing results from the same stations for the different directions. For each azimuth range at each station, we require at least two receiver functions to estimate σ_i. We use a constant value of σ_i for each receiver function gather based on the standard deviation of receiver function amplitudes averaged over all time samples in the trace. The restriction to a minimum of 2 receiver functions gives a total of 890 inversions. For each inversion we stack the receiver functions in slowness bins of 0.005 s/km to reduce the computation time, weighing the misfit function of each stack by the number of traces in it. We then perform the joint inversion using the phase velocities and initial model corresponding to the closest grid cell. Velocity model weighting is adjusted so that velocities for $z \geq 150$ km do not change from the initial model, promoting the interpretation of later receiver function spikes as multiples of shallower discontinuities. We also find that for the joint inversions a damping factor of $\gamma = 0.5$ produces slightly more stable results. We evaluate the inversion result after 30 iterations for $p = 0.1, 0.2,.,0.9$, then select the result that produces the minimum misfit to the receiver functions while satisfying constraints for the maximum allowed change from the initial model. Specifically, we require that the standard error (average of the residual misfits normalized by the standard deviations) of the phase velocity fit cannot increase by more than 0.1, and that the depth-averaged absolute difference between the initial and final V_S models cannot increase by more than 0.1 km/s. These constraints were determined by a trial and error approach for a random sample of 20 stations. Use of the average absolute difference invokes less of a penalty for sharp discontinuities than the average squared difference. If neither of the above constraints can be satisfied with a receiver function misfit that is less than 30%, we discard the inversion result. This gives a total of 698 successful inversions where 513 are computed with $p = 0.1$. Our method of evaluating joint inversions is illustrated for a single gather containing 3 receiver function stacks (SW direction of station TUC from the US network, located in the SBR region) in Figure 3. This illustrates a case where the phase velocity standard error constraint is not satisfied at $p = 0.1$. The result for $p = 0.3$ is chosen as the final result because it has the lowest receiver function misfit where all constraints are satisfied.

4. Joint Inversion Results

4.1. Individual Profiles

[17] A comparison between data and synthetics is shown for all gathers of six example stations in Figure 4 with the location of these stations noted in Figure 1. These examples illustrate that the inversions often fit the receiver functions by incorporating sharper V_S gradients in the crust at $z \approx 10$ km and a strong positive gradient corresponding to the Moho at 25–45 km depth. In addition, the results for stations WUAZ, ISCO and ANMO (Figures 4c, 4d and 4f which are in the CP, RM and RGR regions, respectively) show consistent evidence for sharp V_S changes within the high V_S part of the mantle lithosphere. The only station showing an increased negative gradient above the mantle low velocity zone (LVZ) that could be interpreted as the base of the lithosphere is ELK (Figure 4a) in the NBR region. Station SRU (Figure 4b), in the northern part of the CP region, shows a case where the Moho signal is fairly weak and therefore results in a more gradual change in V_S.

[18] The results for the crustal layers are dominantly sensitive to the amplitude of the receiver functions at $t = 0$ and a common negative spike that immediately follows. These results show notable variations between the azimuth gathers for individual stations indicating the possible presence of anisotropic structure such as dipping layers. However, signals directly after $t = 0$ can be sensitive to uneven topography and the band-pass filtering. Hence, we do not place too much significance on the discontinuities imaged in the crust.

[19] These examples also illustrate a number of later spikes in the receiver function ($25 \lesssim t < 50$ s) traces that cannot be reconciled with the phase velocity data. In our results we interpret such signals as a result of seismogram noise, but they may also relate to unmodeled complexity from sedimentary basins and nearby topography.

4.2. Regional Results

[20] The inversion results are combined to generate a 3-D image of V_S in Figure 5. The location of unsuccessful inversions where the receiver functions and phase velocities could not be reconciled within our constraints are indicated

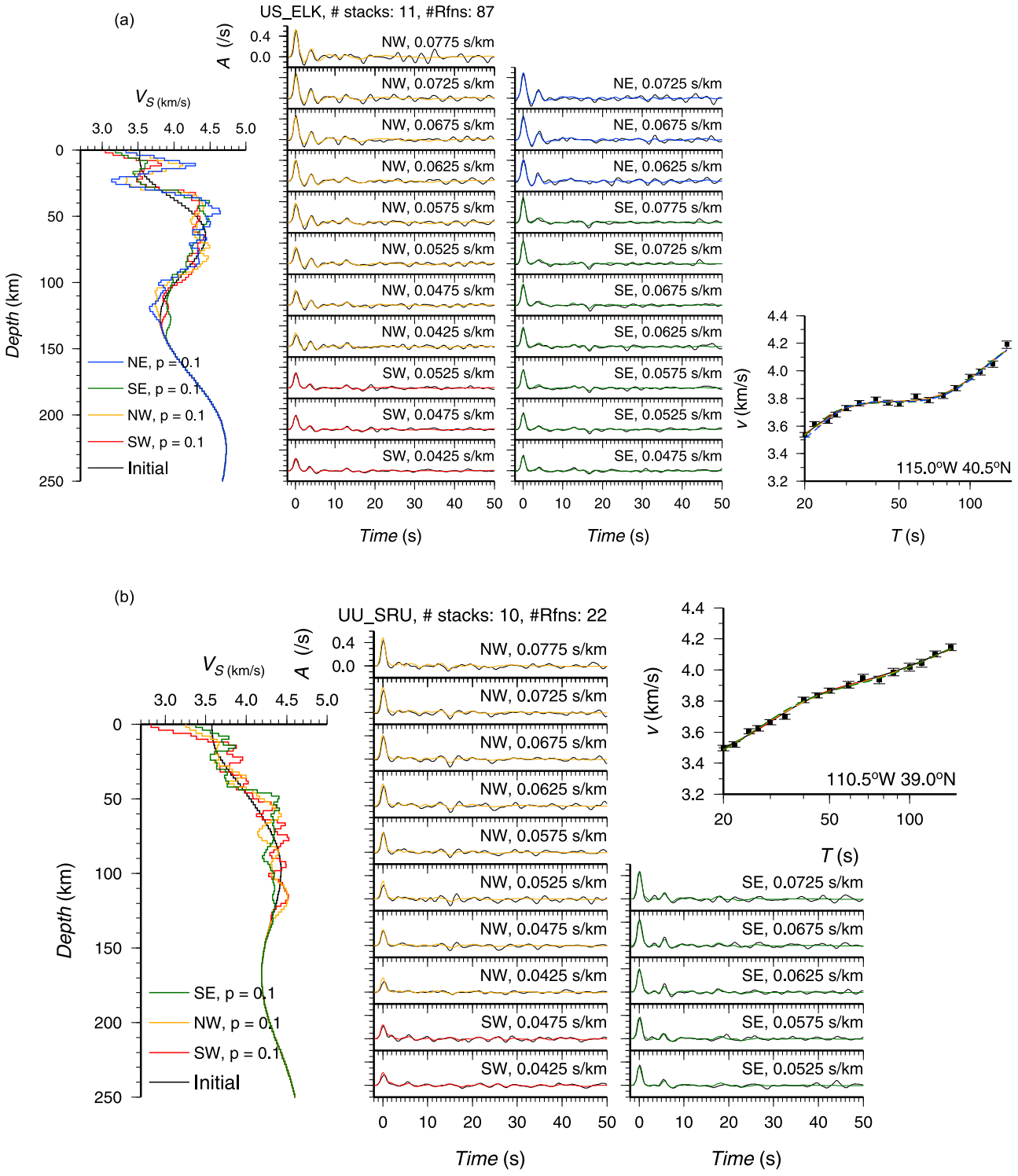

Figure 4. Joint inversion results from six example stations shown in terms of the V_S profile as well as fits to the receiver function and phase velocity data. The six stations are (a) US-ELK in the NBR region, (b) UU-SRU in the northern part of the CP, (c) US-WUAZ in the southern part of the CP, (d) US-ISCO in the eastern part of the RM region, (e) US-TUC in the eastern part of the SBR region, and (f) IU-ANMO in the northern part of the RGR region. Black lines in the V_S profiles show the initial model obtained from a phase velocity inversion. Colored lines show the final model from inversion of each back azimuth group. The same colors are used to show corresponding synthetic receiver functions and phase velocities. These synthetics overlay the data shown by black lines in the case of the receiver functions and black dots with error bars in the case of the phase velocities.

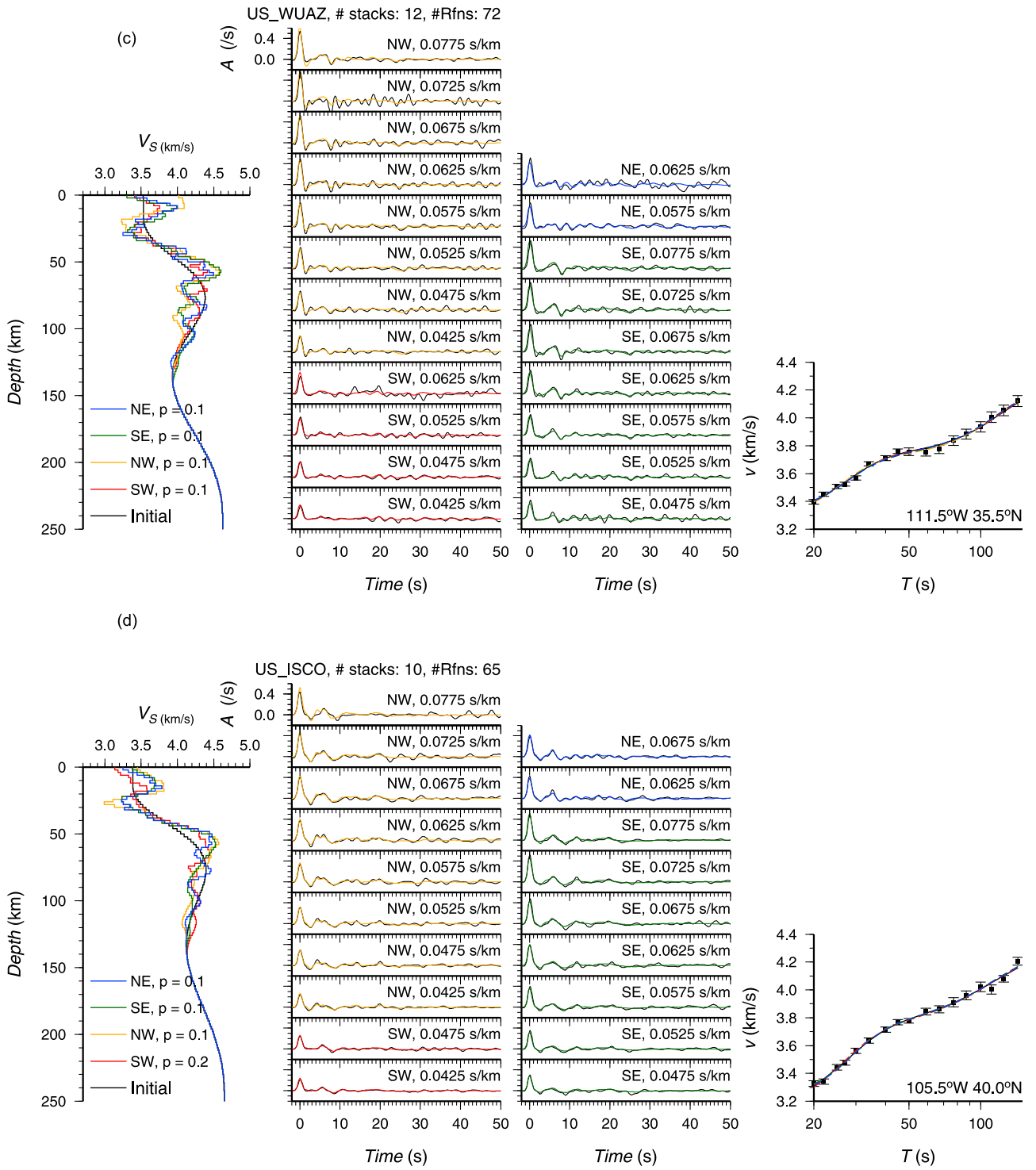

Figure 4. (continued)

by red dots. The notable number of failures to find a solution in the SE of the CP may relate to complications from the presence of localized partial melt beneath the Jemez Lineament [e.g., *Spence and Gross*, 1990]. We also find a larger proportion of unsuccessful inversions in the northern part of the RM region, which are likely to be related to the effects of dipping structure and uneven topography on the receiver functions, both of which are not incorporated into the generation of synthetic seismograms.

[21] We compare the joint inversion results to the 1-D TNA model of *Grand and Helmberger* [1984] in Figure 6 using the same cross sections as for the receiver function

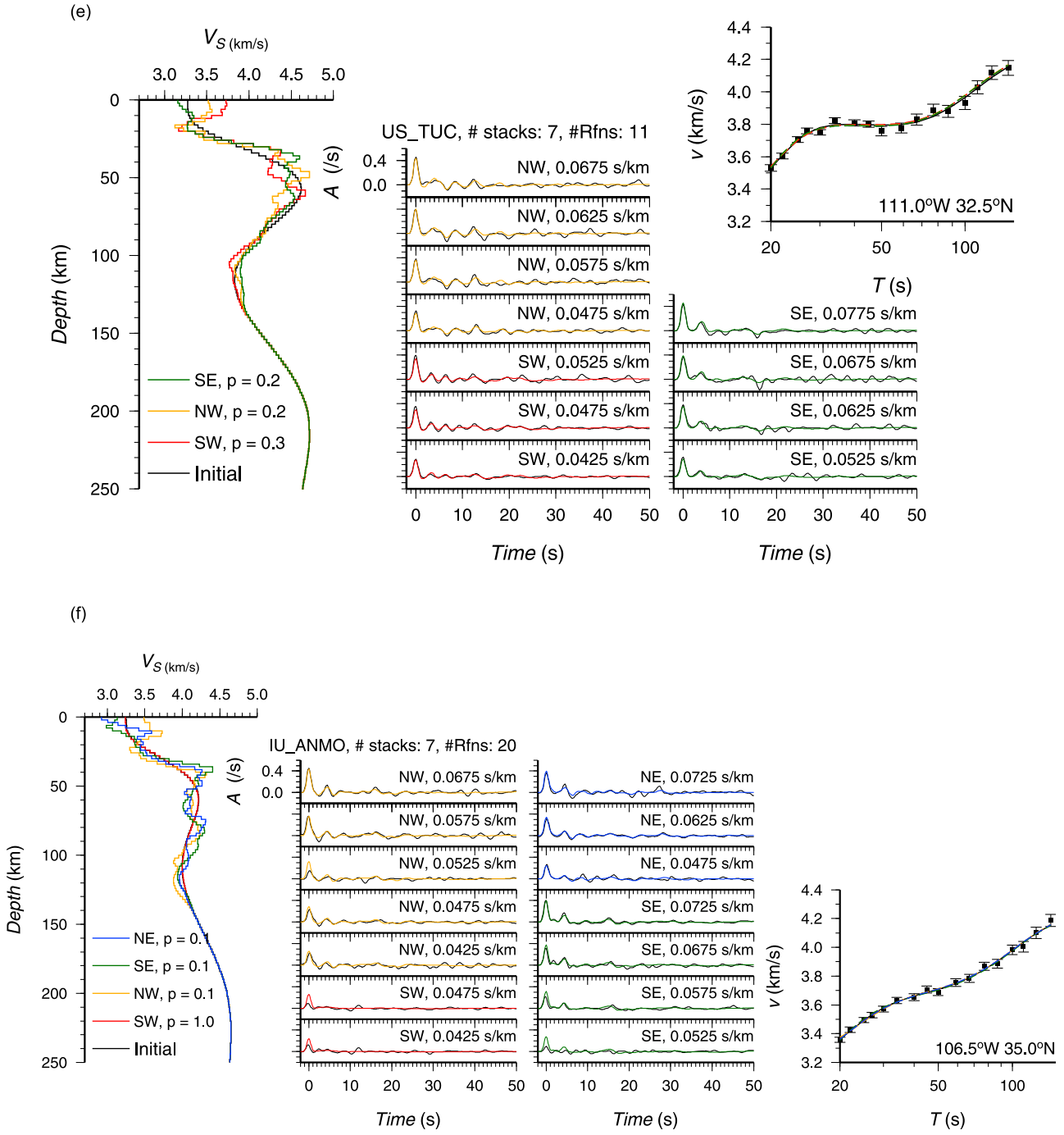

Figure 4. (continued)

profiles in Figure 2. Combined with Figure 5, these results show three subsurface features that apparently correlate with the surface definition of the CP: (1) relatively fast crustal velocities (z = 13 km), (2) a sharp change in crustal thickness along the western, southern and southeastern boundaries, and (3) a high velocity feature in the lithospheric mantle beneath the center of the CP and RM to the north (71 $\lesssim z \lesssim$ 120 km).

[22] As with the example inversions, we find a general tendency for a low velocity zone in the lower crust and in some cases unreasonably high V_S in the upper crust, both of which are possibly related to poorly modeled near-surface effects. Nevertheless, some of these signals may relate to a proposed mafic lower crust in the CP [e.g., *Zandt et al.*, 1995] which can also explain the weaker Moho signal in some parts of the CP (e.g., Figure 2c). In addition, anomalously slower velocities (V_S < 3.3 km/s) in the z = 13 km slice and in both cross sections tend to concentrate at the CP boundaries. These concentrations of low velocity correlate with locations of Cenozoic magmatism [*Roy et al.*, 2009].

[23] The change in crustal thickness is illustrated clearly in the 29 and 33 km depth slices showing faster (~4.0 km/s) mantle velocities beneath the NBR and SBR provinces

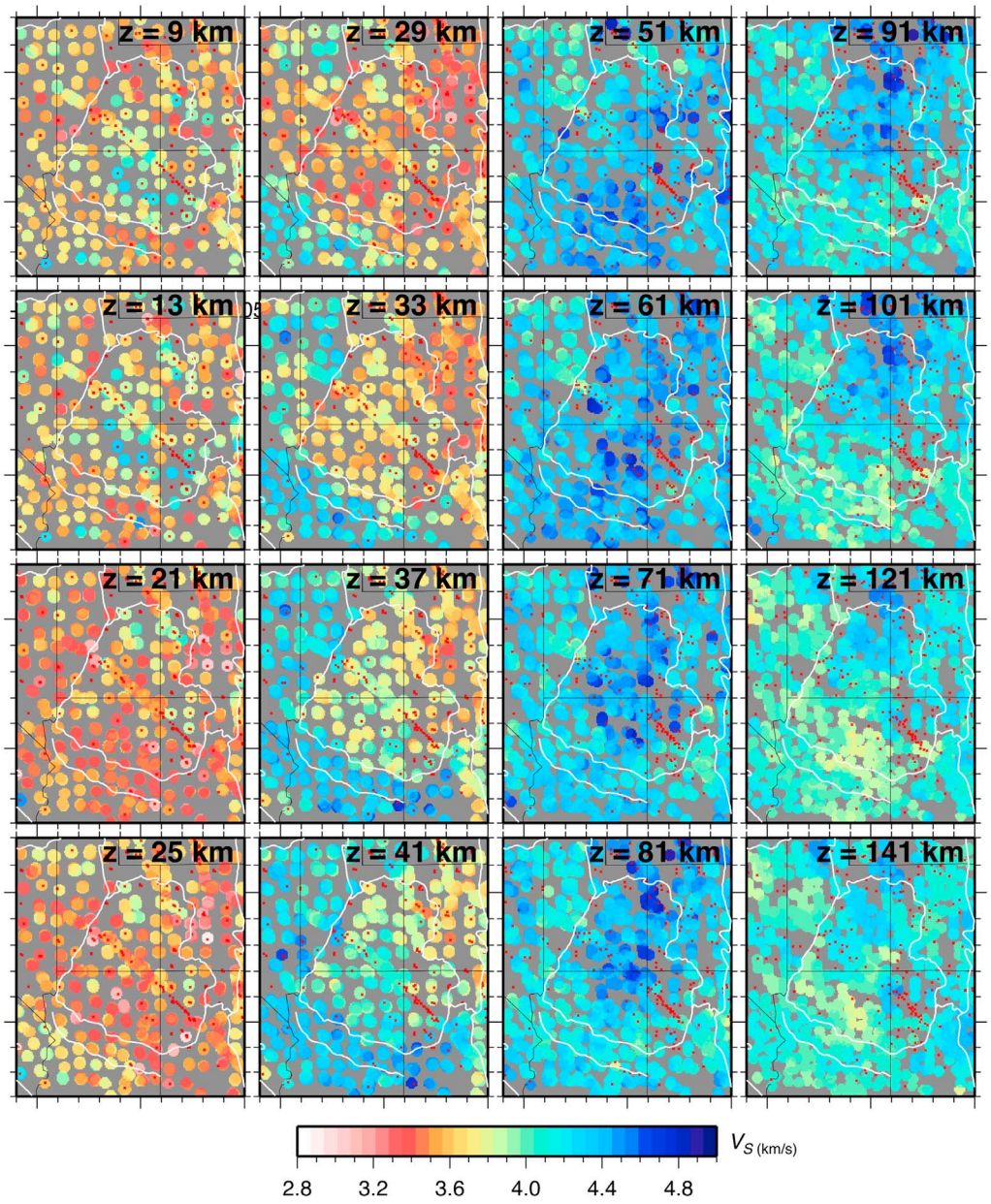

Figure 5. A selection of depth slices at varying intervals of 4–20 km showing the compiled V_S joint inversion results horizontally convolved with a 50 km radius box car function. Red dots indicate the locations of inversions where the receiver functions and phase velocities could not be reconciled within our constraints for misfit. White lines show the tectonic province boundaries and black lines show the state boundaries.

sharply changing to slower (~3.6 km/s) crustal velocities exactly beneath the CP boundary. The 37 km depth slice shows a similar sharp change between the RGR/CP and RGR/RM boundaries. The Moho depth map in Figure 7a is based on depths where V_S jumps from <3.8 km/s to >4 km/s over a depth interval of ≤6 km. The result is similar if we select the depth where the velocity gradient is largest. This illustrates the sharp change in crustal thickness that follows the boundary of the CP with the NBR, ATZ and RGR. At the northeastern boundary of the CP with the RM there is a crustal thickness increase, though this is not as sharp as for the other boundaries. Within the interior of the CP, the estimated Moho depth varies from ~35–46 km. Results where there is no strong Moho signal, shown by crosses in Figure 7a, are much more common beneath the CP than other regions. In addition, there is ambiguity for some V_S profile results where multiple depths satisfy the conditions for the estimated Moho. This is notable in the west of the CP on the NW-SE cross section (111.5°W,38°N, Figure 6), where the low dV_S above higher dV_S within the mantle is consistent with the results of *Levander et al.* [2011] in relation to ongoing delamination.

[24] The high velocity anomaly beneath the CP in the depth range ~70–100 km is roughly coincident with the

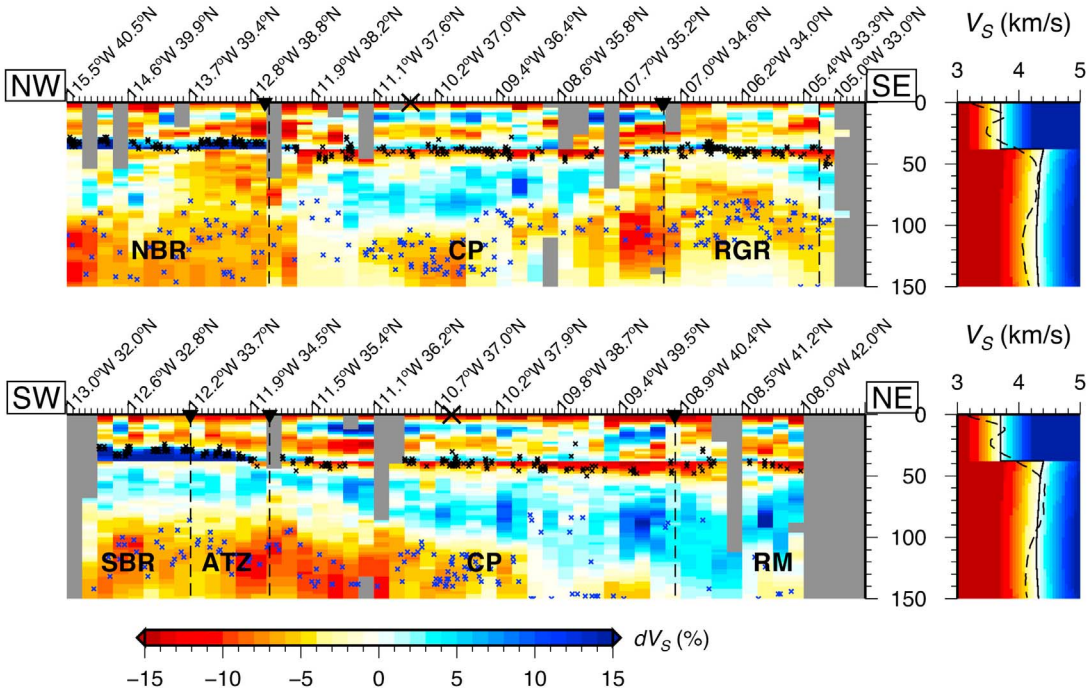

Figure 6. Cross-sections through the 3-D V_S model (Figure 5) along profiles shown in Figure 2. The cross-sections are computed by averaging V_S results over a grid with dimensions of 25 km along the profile, 2 km in depth, and 200 km perpendicular to the profile. The color scale represents $\delta V_S = 100 V_S / V_S^{ref}$ where V_S^{ref} is the TNA model [*Grand and Helmberger*, 1984] shown by the solid line in the profiles to the right of each section. Black dashed lines in the profiles show the 1-D average along each of the cross-sections. Black and blue crosses show the estimated Moho and LVZ depths, respectively, estimated for each inversion result as outlined in the text.

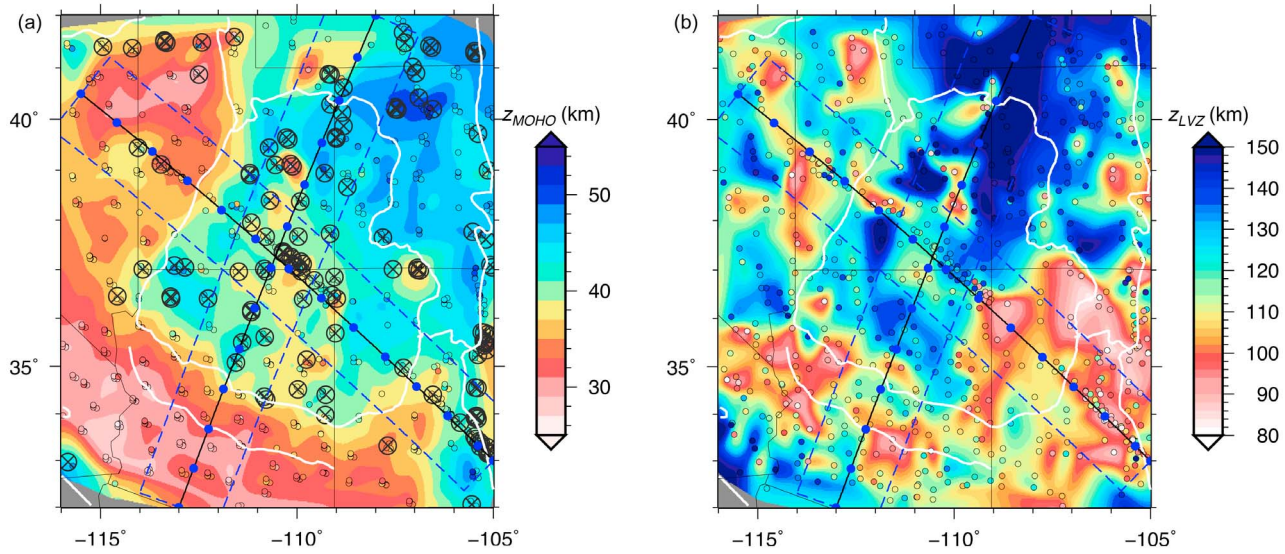

Figure 7. Depth to the (a) estimated Moho and (b) estimated mantle low velocity zone based on the joint inversion V_S results. The individual estimates at the location of their Ps conversion point are shown by colored circles. These results are triangulated and convolved with a Gaussian filter using GMT [*Wessel and Smith*, 1998] to generate the background colors. In Figure 7a, crossed circles indicate the locations where no Moho estimate was made because the V_S gradient was too low. Blue dashed lines indicate the cross-sections used in Figures 2 and 6. White lines show the tectonic province boundaries.

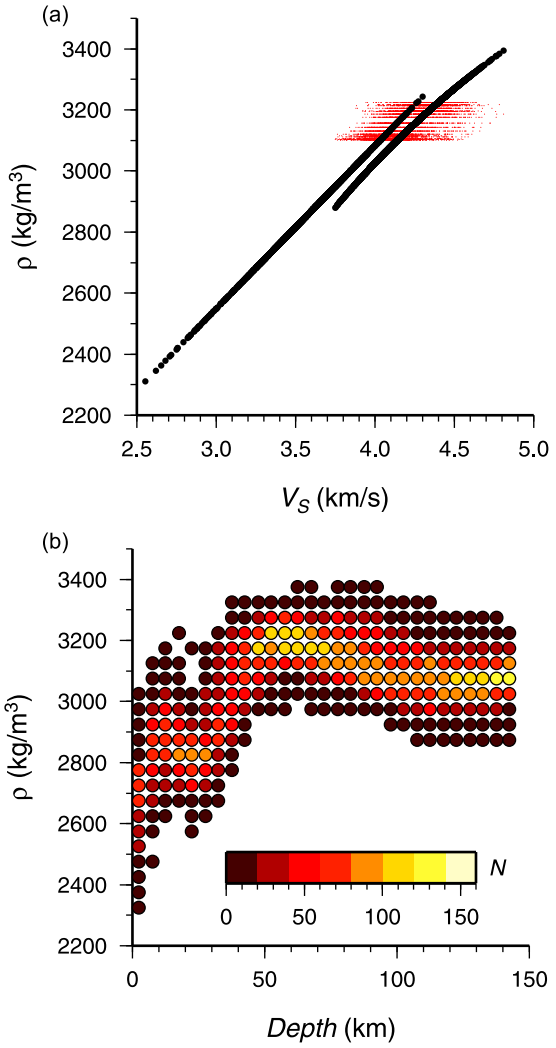

Figure 8. (a) Shear wave velocity versus density for each prism of the gridded model (black dots) using separate scaling relations above and below the crust based on *Christensen and Mooney* [1995]. The distinct lines show the separation into crust and mantle scaling relations used. Red dots indicate the change in scaling relations if densities are laterally homogeneous for all layers below z = 50 km. (b) Distribution of density with depth for the entire gridded model. Color indicates the number of grid prisms with each particular depth and density.

center of the plateau, but thickens beneath the RM to the north (Figure 6). We map the base of this anomaly by computing the depth to the lowest V_S beneath the estimated Moho in each profile (Figure 7b). We note that the depth increase of this low velocity zone (LVZ) shows a more northerly trend into the RM than the northeasterly increase in crustal thickness (Figure 7a). In the southeast of the region, the LVZ depths are relatively shallow, corresponding to potentially thin lithosphere beneath the RGR [e.g., *West et al.*, 2004]. For the NBR region, LVZ depth estimates can be quite variable due to relatively low V_S at all depths below the Moho.

[25] We interpret the LVZ in terms of the lithospheric thickness, but do not find strong evidence for a localized seismic discontinuity above it. This is likely to be influenced by receiver function signals from a sharp boundary being overshadowed by Moho reverberations arriving at similar times. Results for a seismic discontinuity above the LVZ based on S to P conversions [*Levander et al.*, 2011], which arrive before the multiples, are slightly higher than our LVZ depth estimates.

5. Prediction of Gravity Anomalies From V_S Results

[26] As an independent test of our inversion results, we consider the gravity anomaly predicted after mapping V_S to density, then compare this with observed Bouguer anomalies. We first generate a 3-D V_S model by linear interpolation of the collection of 1-D inversion results to a 0.5° × 0.5° × 5 km grid in the top 150 km of the entire region. This leads to a reduction in the extent of the region considered so that we may interpolate to all points. The interpolation is performed separately above and below the estimated Moho surface (Figure 7a) so that we do not introduce additional smoothing across the discontinuity. We convert V_S to V_P using a fixed ratio of V_P/V_S = 1.8 above the Moho, and 1.7 below the Moho. We then convert V_P to ρ using two of the empirical scaling relations of *Christensen and Mooney* [1995]: $\rho[kgm^{-3}] = 947.3 + 296.6V_P$ above the Moho and $\rho[kgm^{-3}] = 5212 - 14{,}863/V_P$ below the Moho. The scaling relations are illustrated in Figure 8a, and the range of densities predicted at each depth level is shown in Figure 8b.

[27] In order to predict the gravity anomalies due to our inferred density distribution, we first approximate the geometry of the model space with a Cartesian grid. The coordinate transformation is based on the horizontal dimensions of a 0.5° × 0.5° grid cell at the surface for a latitude of 0.5°N. This results in a representation of the subsurface by a 3-D grid of constant density cuboids. Several similar solutions for the gravity due to a constant density cuboid exist and we use that of *Okabe* [1979], which we have found to be slightly more numerically stable. We estimate the local gravity anomaly dg at the surface of the grid by summing the contributions from density anomalies $\Delta\rho_{ijk} = \rho_{ijk} - \rho_k^{avg}$ in each prism, where ρ_{ijk} is the density of the prism and ρ_k^{avg} is the average for the layer. This assumes that the subsurface beyond the boundaries of our region can be approximated by a stack of infinite horizontal slabs with densities ρ_k^{avg}. The computed gravity anomalies therefore represent the gravity relative to a regional average, rather than the gravity relative to a reference geoid described by the Bouguer gravity anomaly dg^{BA}. For this reason we subtract the spatial average of the observed Bouguer anomalies when comparing to our predicted anomalies. We refer the observed Bouguer anomalies minus the spatial average as adjusted Bouguer anomalies.

[28] The results of our initial calculation are shown in Figure 9b, as compared to the observations in Figure 9a. The predicted gravity anomalies differ from the observed anomalies by two dominant features: First, the predicted anomalies are dominated by a large positive signal in the north of the CP, corresponding in spatial extent to the fast V_S anomaly imaged at $z \approx 91$ km in Figure 5. In the Bouguer anomaly data there is no obvious signal from this structure, and the spatial distribution dominantly reflects the crustal thickness map in Figure 7a. Secondly, the range in predicted

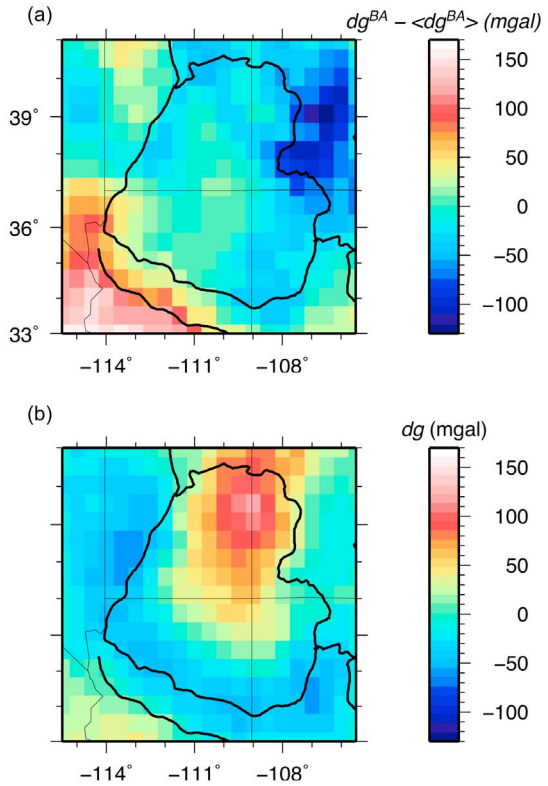

Figure 9. (a) Distribution of Bouguer gravity anomalies across the study region minus the spatial average. Values are taken from the US gravity database and averaged on a 0.5° grid. (b) Predicted gravity anomalies due to the distribution of calculated density in the top 150 km beneath the region. Black lines show the tectonic province and US state boundaries.

anomalies is ∼180 mgal, which is smaller than the observed range of ∼290 mgal. Both differences suggest that our calculation of gravity anomalies overemphasizes the influence of density variations in the mantle and under-emphasizes variations closer to the Moho.

[29] We assess the importance of mantle density variations with respect to *dg* by recomputing the anomalies using only densities of grid points above a threshold depth z_{MAX}. For each z_{MAX} we evaluate the RMS fit to the adjusted Bouguer anomaly (Figure 10a). This shows that the predicted anomalies best match the observations when we ignore all density variations below 50 km. The example maps of *dg* in Figures 10b and 10d show that when z_{MAX} = 30 km the signal is dominated by a higher relative density of the CP crust and when z_{MAX} = 75 km the signal shows a large positive signal due to higher density in the lithospheric mantle. When z_{MAX} = 50 km (Figure 10c) there is a balance of contributions from variations in the crustal thickness and the lateral variations in the upper part of the lithospheric mantle, such that negative anomalies are computed throughout the RM region and along the northwest boundary of the CP. However, all three examples, shown with the same color scale as for the observations in Figure 9, illustrate that the range in predicted *dg* is about half of that which is observed. Figure 8a shows the range of V_S if we set a constant density for each layer below 50 km.

[30] Figure 11 shows profiles of the gravity anomalies following the same paths as the cross-sections in Figures 2 and 6. We compare the Bouguer gravity anomaly data points, shifted by removing the spatial average, to the *dg* predictions based on the initial $V_S - \rho$ scaling (z_{MAX} = 150 km) and the cases where z_{MAX} = 30, 50 and 75 km. This illustrates the poor fit of the initial prediction to the north of the CP and in the ATZ. For the three models with $z_{MAX} \leq$ 75 km, we illustrate the improvements to the fit of gravity variations in all regions. The z_{MAX} = 50 km result performs best since the shallower z_{MAX} = 30 km calculation underpredicts the anomaly in the ATZ, while the deeper z_{MAX} = 75 km calculation over-predicts the anomaly in the CP. However, the lack of fit to the range in observed anomalies is illustrated by the lack of a strong positive anomaly in the SBR. In addition, none of the models predict the local reduction in *dg* beneath 108.6°W/35.2°N, where *Roy et al.* [2005] modeled the gravity using a series of 2-D profiles with strong lateral variations in density.

6. Discussion

6.1. Joint Inversion Method

[31] Although there are several previous studies that apply a linearized joint inversion approach using Rayleigh wave and receiver function data [e.g., *Julià et al.*, 2003; *Yoo et al.*, 2007; *Tokam et al.*, 2010], our method is unique in terms of our method for selecting the relative influence parameter *p*. Previous studies selected *p* and the inversion damping parameter γ by trial and error, based on a judgment of relative data quality and appropriate level of complexity in the model. Here, we take advantage of the more stable phase velocity data to choose γ and obtain an initial V_S model. We then solve the inverse problem for a range of *p*, selecting the result based on criteria for minimum allowed misfit to each data type and maximum allowed difference between surface wave and joint inversion results. This allows us to take into account the variable quality of the receiver function data, which may not be captured by our estimated uncertainty. The criteria for maximum allowed difference between the initial phase velocity based model and final model allows us enforce authority of the phase velocity data in constraining the absolute values of V_S and allow the receiver functions to image discontinuities. Genetic algorithms have been successfully applied to similar joint inversion problems and can avoid dependence on an initial model, damping or relative influence parameter [e.g., *Lawrence and Wiens*, 2004; *Moorkamp et al.*, 2010]. However, this approach will lead to a range of acceptable solutions, and in order to combine results into a 3-D model we must make similar decisions in order to choose the best solution.

[32] Following *Tokam et al.* [2010] our approach solves for 1-D velocity models specific to back azimuth bins of stacked receiver functions. An approach that solves for a single 1-D V_S model beneath each individual station disregards the spatially biased sampling that is commonly associated with receiver functions. Separating the receiver function data based on back azimuth allows us to check for potential anisotropy in the results and gives better horizontal resolution for our final velocity results. When combining the 1-D results into a 3-D image, the separate profiles for different azimuths can take advantage of the crossing raypaths

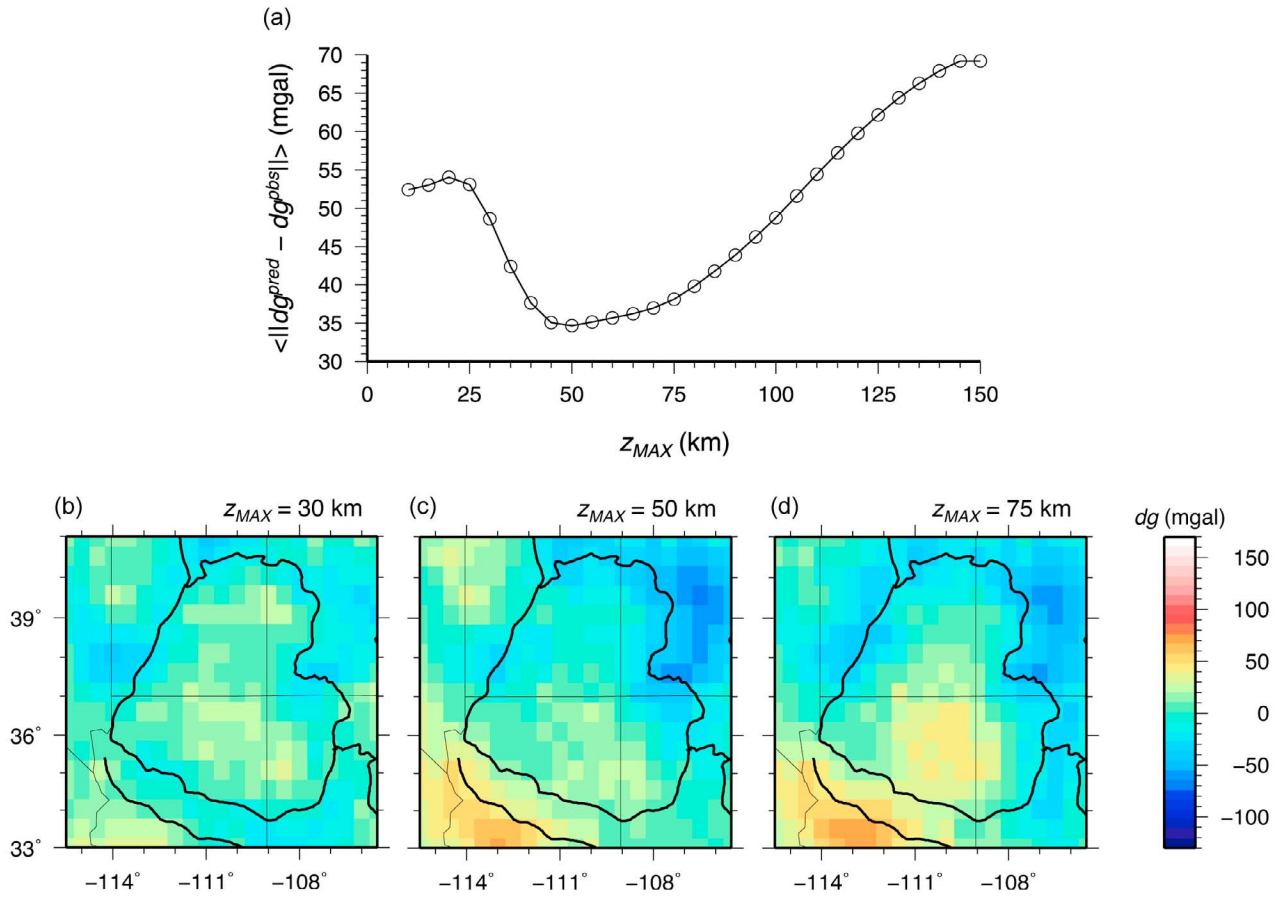

Figure 10. (a) Average misfit of the predicted density anomalies to the adjusted Bouguer anomalies as a function of the maximum depth considered in the gravity anomaly calculation z_{MAX}. (b) The predicted anomalies when z_{MAX} = 30 km. (c) The predicted anomalies when z_{MAX} = 50 km. (d) The predicted anomalies when z_{MAX} = 75 km.

associated with closely spaced stations. Combining a set of 1-D V_S models to generate a 3-D model is inferior to solving the whole problem in 3-D. However, solving a linearized 3-D inversion for this many receiver function data is computationally unfeasible, and the variation in the independent solutions to a number of overlapping 1-D models provide a useful measure of uncertainty. The estimated Moho depth variation (Figure 7a) is similar to other receiver function studies that simultaneously solve for depth and V_P/V_S [*Crotwell and Owens*, 2005; *Wilson et al.*, 2010], providing an independent check on part of the results. We therefore view our approach as a valid estimate of the 3-D structure.

[33] Limitations in the method are highlighted by our inability to reconcile the two data sets in some locations. This is likely to be related to assumptions made in our model setup. For example, we assume basis functions representing the model space as isotropic, constant velocity, constant thickness, horizontal layers, a constant V_P/V_S ratio, a smooth velocity model, and a great circle path of the P-wave between source and receiver. The existence of anisotropic or dipping structure can have strong effects on receiver functions that would not be captured by our model [e.g., *Nagaya et al.*, 2008], but previous studies have indicated that anisotropy is not large beneath the CP [*Savage and Sheehan*, 2000]. We find some possibly spurious results for the crustal layers, where it is important to have good constraint because of reverberations affecting later parts of the receiver functions. There is little constraint provided by the phase velocities to results for the crust, which may be improved by incorporating higher frequencies obtained from ambient noise analysis. Future improvements may be possible by better incorporating near surface and basin effects into the receiver function modeling, and assessing the effects of uncertainties in basis functions by taking an approach such as *Bodin and Sambridge* [2009] that more fully explores the model space.

[34] Horizontal resolution of the final model is limited by smoothing inherent to the phase velocity data and the combined Fresnel zone of all receiver functions. We have not investigated the horizontal resolution fully, but we may expect that structures with lateral size <50 km may not be well imaged within the model due to sparse sampling of receiver functions at shallow depths and broad sensitivity of the phase velocities deeper. However, some resolution is recovered by the localized sampling of the receiver function data, such that we can constrain some sharp horizontal changes such as seen on the western boundary of the CP. Better horizontal resolution at depth could be obtained by incorporating body wave data into the joint inversion.

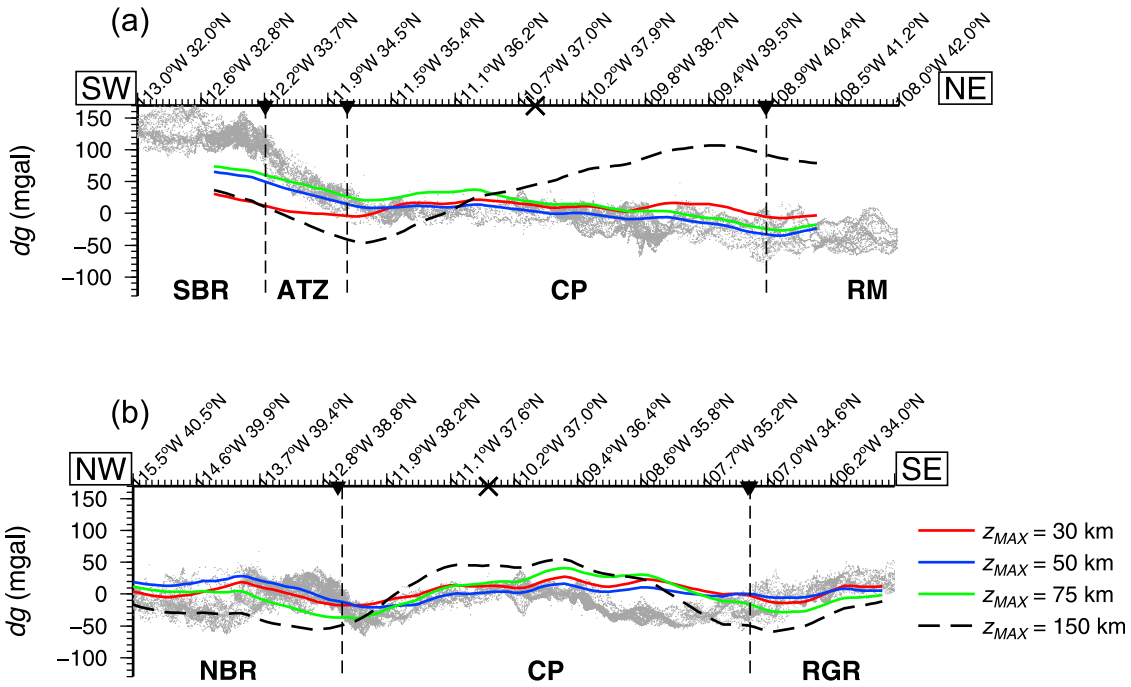

Figure 11. (a and b) Observed Bouguer anomaly values minus the spatial average (gray dots) for the profiles used to generate cross sections in Figures 2 and 6. Lines show the predicted gravity anomalies when considering only densities above specified depths. The depth constraints correspond to the results shown in Figures 9 and 10.

6.2. Gravity Modeling

[35] Discrepancies in the predictions of gravity data based on seismic results have been pointed out before by *Barton* [1986], who showed that the scatter in experimental data used to constrain velocity-density scaling relations is so large that velocity results can be reconciled with a wide range of Bouguer anomaly values. It is likely that the uncertainty related to such scatter is also a factor in the discrepancies between observed and predicted anomalies shown here. Although, gravity data has been successfully incorporated into joint inversions for V_S [e.g., *Maceira and Ammon*, 2009], such inversions are likely to be limited by uncertainty in the velocity-density scaling relations. Future approaches may benefit from fitting the scaling relations to the experimental data as part of the joint inverse problem.

[36] Our gravity modeling results suggest that there are negligible lateral variations in density below z = 50 km. To accommodate this within the mantle scaling relation $\rho = a + b/(\kappa V_S)$, where κ is the V_P/V_S ratio, would require changes in b/κ that are systematically tied to changes in V_S. The parameter ranges for this are not completely unreasonable (e.g., a variation of $1.55 \lesssim \kappa \lesssim 1.85$ could account for the most of the change in density) but the systematic coupling between V_S and κ would be unusual. Our gravity model is unable to fit the range of values in the observed Bouguer anomaly map, notably the highest values to the SW of the region and lowest values in the RM. This may in part be due to lateral variations in the scaling relations which are not considered, but may also relate to roughness damping in the inversions, which reduces the sharp change in density we expect at the Moho. In addition lower resolution at depth of the phase velocities may smear out some of the mantle velocity anomalies, overemphasizing their size and therefore predicting a stronger gravity signal. Nevertheless, the observation that a strong fast anomaly in the lithospheric mantle beneath the CP does not produce a signal in the gravity data provides evidence for a relatively buoyant lithospheric root.

6.3. Structure Beneath the Colorado Plateau

[37] High crustal V_S values for the CP interior relative to low values at its boundaries are consistent with results from ambient noise tomography [*Moschetti et al.*, 2010]. The high V_S values may be explained by cold temperatures consistent with low heat flow measurements [*Blackwell and Richards*, 2004], but may also relate to a dominance of mafic rocks which lead to a stronger CP crust [*Zandt et al.*, 1995]. As in previous receiver function based studies [e.g., *Frassetto et al.*, 2006; *Gilbert et al.*, 2007; *Wilson et al.*, 2010], we find discontinuities within the CP crust that are not observed in neighboring regions and can be interpreted as evidence for strong crustal layers. Mafic rocks in the crust with higher velocity to density ratios [*Christensen and Mooney*, 1995] may also explain why there is no signal of a higher density crust in the observed gravity anomalies. At the CP boundaries low V_S patches correspond to recent volcanism that bounds the CP [*Roy et al.*, 2009], and low densities may relate to basalt depletion [*Roy et al.*, 2005].

[38] Our V_S results are consistent with several previous studies. The Moho depth estimates across the region are generally consistent with automatically computed results from USArray data [*Crotwell and Owens*, 2005] and LaRiSTra results [*Wilson et al.*, 2010] which both solve simultaneously

for crustal thickness and V_P/V_S. Slower mantle velocities beneath the NBR and RGR are also observed in body wave tomography results [*Sine et al.*, 2008] and surface wave tomography results [*West et al.*, 2004] from the LaRiSTra profile, which is roughly equivalent to our NW-SE profile in Figures 2 and 6. A thicker lithosphere beneath the CP is also imaged in surface wave results of *West et al.* [2004] and *Liu et al.* [2011]. We image decreases and increases in V_S that corresponds to delamination of the lithosphere beneath the western CP, as proposed by *Levander et al.* [2011]. There is some indication that this links continuously with a strong localized high velocity feature at $z \approx 150$ km that is observed in Western US body wave models [e.g., *Schmandt and Humphreys*, 2010; *Obrebski et al.*, 2011; *Sigloch*, 2011]. However, the variability of inversion results is high in this region, indicating that dipping layers may play a role.

[39] Results requiring 50 km of density variations to explain the gravity anomalies are consistent with previous isostatic calculations that indicate some support of CP elevations from a lower density mantle [e.g., *Lastowka et al.*, 2001; *Wilson et al.*, 2010]. This effect is more pronounced beneath the NBR and RGR where we find lower values of V_S and density in the lithospheric mantle that compensate for a relatively thin crust. A generally low density lithosphere is consistent with the hydrated lithosphere hypothesis of *Humphreys et al.* [2003], and an average free air anomaly close to zero implies that much support for the region is provided by static lower density features in the lithosphere.

[40] Our results indicate that the CP is unique due to a combination of crust and lithospheric mantle properties. The sharp changes in crustal thickness show a distinction between the CP and the provinces dominated by extensional tectonics (NBR, SBR and RGR). However, there is no similar change at the eastern/northeastern boundary with the RM where crust thickens more gradually. This indicates that dominant signals in crustal thickness results relate to post-Laramide extension in the western US. A high V_S anomaly indicates that lithospheric mantle beneath the central CP is unique relative to all surrounding regions except the part of the RM to the north. The lack of a gravity anomaly signal from this lithospheric root indicates that it may be largely neutrally buoyant, as suggested by *Roy et al.* [2009]. Xenolith evidence suggests a Proterozoic origin to the CP lithosphere [*Bowring and Karlstrom*, 1990], but continuation of the V_S anomaly to the north suggests a connection with the Wyoming Craton. Low heat flow through a stable lithospheric mantle could lead to a relatively cold and therefore strong crust, explaining higher V_S without the need for a mafic lower crust. Observations of low crustal V_S in areas of Cenozoic volcanism around the boundaries of the CP, where the lithospheric root is not observed, lend support an idea that the central CP is relatively cool due to its thicker lithosphere.

[41] Regardless of the mechanism, a strong crust can explain a resistance to compressional deformation during the Laramide orogeny. Slow V_S beneath the NBR, SBR, RGR and southernmost RM is consistent with a model that suggests past lithospheric removal replaced by hot asthenosphere [e.g., *Bird*, 1988] or significant geochemical alteration of the lithosphere [*Humphreys et al.*, 2003] associated with flat slab subduction and/or subsequent break-off of the slab. In contrast, there is little evidence for large-scale lithospheric removal beneath the CP as a mechanism for its uplift [*Morgan and Swanberg*, 1985; *Spencer*, 1996]. The resultant lithospheric mantle heterogeneity may have promoted a weaker crust in the neighboring NBR, SBR and RGR and can explain how post-Laramide extension and magmatism has not occurred in the CP, leading to the sharp change in observed crustal thickness at the west, south and southeastern CP boundaries. Furthermore, the differential heating of the heterogeneous lithosphere can explain the CP uplift [*Roy et al.*, 2009].

[42] Current support for the CP can be explained by a combination of thickened crust, low density lithospheric mantle, and possible ongoing attenuation at the CP edges [*van Wijk et al.*, 2010; *Levander et al.*, 2011]. The thickened crust compensates for the higher density of lithosphere relative to the neighboring NBR, where the Bouguer anomaly values are similar. *McQuarrie and Chase* [2000] have argued that the CP crust must have been thinner when at sea level during the early Laramide orogeny, and suggested a thickening mechanism by mid-crustal flow from the previously higher topography of the Sevier orogeny to the west. However, that model requires a balance between strength in the crust required to resist large-scale deformation and weakness required to promote previous crustal flow that has not returned to the now lower SBR. Furthermore, we might expect a more marked transition into the crust beneath the RM than is observed. In contrast to the proposed east-west crustal flow, seismic anisotropy from ambient noise tomography has a southwest-northeast orientation for the CP crust [*Lin et al.*, 2011]. An alternative mechanism proposed for crustal thickening is the net transport of material at the base of the crust due to shear stress during flat slab subduction [*Bird*, 1984]. This is more consistent with the direction of crustal anisotropy but inconsistent with our interpretation of a stable lithospheric root, which would act as a barrier to the transmission of shear stress. We could reconcile this with our observation of a high V_S lithospheric root if we interpret it as remnant depleted lithosphere that was also pushed to the northeast by the Farallon slab [*Thompson and Zoback*, 1979]. However, this would require a pre-existing strong crust to have resisted deformation during that time. Without strong evidence to distinguish between a pre-existing thick crust above stable, cold lithosphere and a Laramide-thickened crust above a relocated lithosphere, we favor the former simpler, explanation. Given that *Liu and Gurnis* [2010] model the subsidence and uplift of the CP with a constant thickness lithosphere, it is feasible that the crust and lithosphere thicknesses for the CP have remained largely constant since before the Laramide orogeny.

7. Conclusions

[43] We have demonstrated a method for the joint inversion of Rayleigh wave phase velocity and P receiver function data using a large data set to obtain a 3-D V_S model of a $\sim$10,000 km^2 region including the Colorado Plateau and parts of the surrounding tectonic provinces. Results show a relatively thin crust ($\sim$20–30 km) beneath the Basin and Range, sharply increasing to $\sim$45 km at the boundary with the Colorado Plateau. The crust thickens more gradually to the east and northeast, reaching $\sim$50 km beneath the Rocky Mountains. Lithospheric thickness is less accurately defined

by our results, but there is clear evidence for relatively thick (>100 km) lithosphere beneath the center of the plateau which thickens more to the north beneath the Rocky Mountains. Evidence for thinner (<80 km) lithosphere is found beneath the southernmost Rocky Mountains, Rio Grande Rift and the southeastern part of the Basin and Range, supporting a hypothesis that lithosphere has been either removed or strongly altered in those regions since the time of the Laramide orogeny. Mapping velocity results to density leads to a poor initial fit of observed gravity data. However, reasonable fits can be obtained if lateral density variations at depths greater than 50 km are ignored, indicating that much of the faster lithospheric mantle may be neutrally buoyant. This suggests a long term tectonic stability of the plateau, which in turn could have led to a relatively stronger colder crust that resisted large-scale deformation during and subsequent to the Laramide orogeny. Heterogeneous mantle lithosphere is consistent with an uplift mechanism related to differential heating following removal of the Farallon slab, and ongoing uplift due to small-scale convection and delamination.

[44] **Acknowledgments.** Comments from the Editor Robert Nowack and two anonymous reviewers greatly improved this manuscript. We thank Thorsten Becker for useful discussions, Jim Ni for comments on a draft of the manuscript, and Matthew Fouch for providing COARSE array data before release by IRIS. Joint inversions presented here relied on the codes made available by R. B. Herrmann and C. J. Ammon and we are grateful for this resource. Other Seismic data were obtained from the IRIS Data Management Center, and we are grateful to all investigators involved in collection and processing of these data. All figures and some calculations in this paper make use of GMT software [*Wessel and Smith*, 1998]. This project was largely funded by NSF grants EAR-0844760 and EAR-0844741.

References

Ammon, C. J., G. E. Randall, and G. Zandt (1990), On the nonuniqueness of receiver function inversions, *J. Geophys. Res.*, *95*(B10), 15,303–15,318, doi:10.1029/JB095iB10p15303.

Barton, P. J. (1986), The relationship between seismic velocity and density in the continental crust—A useful constraint?, *Geophys. J. R. Astron. Soc.*, *87*(1), 195–208, doi:10.1111/j.1365-246X.1986.tb04553.x.

Beghoul, N., and M. Barazangi (1989), Mapping high Pn velocity beneath the Colorado Plateau constrains uplift models, *J. Geophys. Res.*, *94*(B6), 7083–7104, doi:10.1029/JB094iB06p07083.

Bird, P. (1984), Laramide crustal thickening event in the Rocky Mountain foreland and Great Plains, *Tectonics*, *3*(7), 741–758, doi:10.1029/TC003i007p00741.

Bird, P. (1988), Formation of the Rocky Mountains, western United States: A continuum computer model, *Science*, *239*(4847), 1501–1507, doi:10.1126/science.239.4847.1501.

Blackwell, D. D., and M. Richards (2004), Geothermal map of North America, 1 sheet, scale 1:6,500,000, Am. Assoc. of Pet. Geol., Tulsa, Okla.

Bodin, T., and M. Sambridge (2009), Seismic tomography with the reversible jump algorithm, *Geophys. J. Int.*, *178*(3), 1411–1436, doi:10.1111/j.1365-246X.2009.04226.x.

Bowring, S. A., and K. E. Karlstrom (1990), Growth, stabilization, and reactivation of Proterozoic lithosphere in the southwestern United States, *Geology*, *18*(12), 1203–1206, doi:10.1130/0091-7613(1990)018<1203:GSAROP>2.3.CO;2.

Christensen, N., and W. Mooney (1995), Seismic velocity structure and composition of the continental crust: A global view, *J. Geophys. Res.*, *100*(B6), 9761–9788, doi:10.1029/95JB00259.

Crotwell, H. P., and T. J. Owens (2005), Automated receiver function processing, *Seismol. Res. Lett*, *76*(6), 702–709, doi:10.1785/gssrl.76.6.702.

Dueker, K., and H. Yuan (2004), Upper mantle P-wave velocity structure from PASSCAL teleseismic transects across Idaho, Wyoming and Colorado, *Geophys. Res. Lett.*, *31*, L08603, doi:10.1029/2004GL019476.

Dutton, C. E. (1880), *Report on the Geology of the High Plateaus of Utah, With Atlas*, Gov. Print. Off., Washington, D. C.

Flowers, R. M., B. P. Wernicke, and K. A. Farley (2008), Unroofing, incision, and uplift history of the southwestern Colorado Plateau from apatite (U-Th)/He thermochronometry, *Geol. Soc. Am. Bull.*, *120*(5–6), 571–587, doi:10.1130/B26231.1.

Forsyth, D. W., and A. Li (2005), Array-analysis of two-dimensional variations in surface wave phase velocity and azimuthal anisotropy in the presence of multi-pathing interferece, in *Seismic Earth: Array Analysis of Broadband Seismograms*, *Geophys. Monogr. Ser.*, vol. 157, edited by A. Levander and G. Nolet, pp. 81–98, AGU, Washington, D. C.

Frassetto, A., H. Gilbert, G. Zandt, S. Beck, and M. J. Fouch (2006), Support of high elevation in the southern Basin and Range based on the composition and architecture of the crust in the Basin and Range and Colorado Plateau, *Earth Planet. Sci. Lett.*, *249*(1–2), 62–73, doi:10.1016/j.epsl.2006.06.040.

Gilbert, G. K. (1875), Report on the geology of portions of Nevada, Utah, California, and Arizona examined in the years 1871 and 1872, in *Report on the U.S. Geographical and Geological Surveys West of the 100th Meridian, in Charge of First Lieut. Geo. M. Wheeler*, vol. 3, pp. 17–187, Gov. Print. Off., Washington, D. C.

Gilbert, H., A. A. Velasco, and G. Zandt (2007), Preservation of Proterozoic terrane boundaries within the Colorado Plateau and implications for its tectonic evolution, *Earth Planet. Sci. Lett.*, *258*(1–2), 237–248, doi:10.1016/j.epsl.2007.03.034.

Gorman, A. R., et al. (2002), Deep Probe-imaging the roots of western North America, *Can. J. Earth Sci.*, *39*, 375–398.

Grand, S., and D. Helmberger (1984), Upper mantle shear structure of North America, *Geophys. J. R. Astron. Soc.*, *76*(2), 399–438.

Henstock, T. J., et al. (1998), Probing the Archean and Proterozoic lithosphere of western North America, *GSA Today*, *8*, 1–5, 16–17.

Hinze, W. J., et al. (2005), New standards for reducing gravity data: The North American gravity database, *Geophysics*, *70*, J25–J32.

Humphreys, E. D. (1995), Post-Laramide removal of the Farallon slab, western United States, *Geology*, *23*(11), 987–990, doi:10.1130/0091-7613(1995)023<0987:PLROTF>2.3.CO;2.

Humphreys, E. D., E. Hessler, K. Dueker, G. L. Farmer, E. Erslev, and T. Atwater (2003), How Laramide-age hydration of North American lithosphere by the Farallon slab controlled subsequent activity in the western United States, *Int. Geol. Rev.*, *45*(7), 575–595.

Huntington, K. W., B. P. Wernicke, and J. M. Eiler (2010), Influence of climate change and uplift on Colorado Plateau paleotemperatures from carbonate clumped isotope thermometry, *Tectonics*, *29*, TC3005, doi:10.1029/2009TC002449.

Julià, J., C. J. Ammon, R. B. Herrmann, and A. M. Correig (2000), Joint inversion of receiver function and surface wave dispersion observations, *Geophys. J. Int.*, *143*(1), 99–112.

Julià, J., C. J. Ammon, and R. B. Herrmann (2003), Lithospheric structure of the Arabian Shield from the joint inversion of receiver functions and surface-wave group velocities, *Tectonophysics*, *371*(1–4), 1–21, doi:10.1016/S0040-1951(03)00196-3.

Karlstrom, K. E., S. J. Whitmeyer, K. Dueker, M. L. Williams, A. Levander, E. D. Humphreys, G. R. Keller, and the CD-ROM Working Group (2005), Synthesis of results from the CD-ROM experiment: 4-D image of the lithosphere beneath the Rocky Mountains and implications for understanding the evolution of continental lithosphere, in *The Rocky Mountain Region: An Evolving Lithosphere—Tectonics, Geochemistry and Geophysics*, *Geophys. Monogr. Ser.*, vol. 154, edited by K. E. Karlstrom and G. R. Keller, pp. 412–434, AGU, Washington, D. C.

Karlstrom, K. E., R. Crow, L. J. Crossey, D. Coblentz, and J. van Wijk (2008), Model for tectonically driven incision of the younger than 6 Ma Grand Canyon, *Geology*, *36*(11), 835–838, doi:10.1130/G25032A.1.

Keller, G. R., et al. (2006), A community effort to construct a gravity database for the United States and an associated Web portal, *GSA Spec. Pap. 397*, pp. 21–34, Geol. Soc. of Am., Boulder, Colo., doi:10.1130/2006.2397(02). [Available at http://irpsrvgis00.utep.edu/repositorywebsite/.]

Kennett, B. L. N., E. R. Engdahl, and R. Buland (1995), Constraints on seismic velocities in the Earth from traveltimes, *Geophys. J. Int.*, *122*(1), 108–124.

Lastowka, L. A., A. Sheehan, and J. M. Schneider (2001), Seismic evidence for partial lithospheric delamination model of Colorado Plateau uplift, *Geophys. Res. Lett.*, *28*(7), 1319–1322, doi:10.1029/2000GL012360.

Lawrence, J. F., and D. A. Wiens (2004), Combined receiver-function and surface wave phase-velocity inversion using a niching genetic algorithm: Application to Patagonia, *Bull. Seismol. Soc. Am.*, *94*(3), 977–987, doi:10.1785/0120030172.

Levander, A., B. Schmandt, M. S. Miller, K. Liu, K. E. Karlstrom, R. S. Crow, C.-T. A. Lee, and E. D. Humphreys (2011), Continuing Colorado Plateau uplift by delamination-style convective lithospheric downwelling, *Nature*, *472*, 461–465, doi:10.1038/nature10001.

Ligorria, J. P., and C. J. Ammon (1999), Iterative deconvolution and receiver-function estimation, *Bull. Seismol. Soc. Am.*, *89*(5), 1395–1400.

Lin, F., M. Ritzwoller, Y. Yang, M. Moschetti, and M. Fouch (2011), Complex and variable crustal and uppermost mantle seismic anisotropy in the western United States, *Nat. Geosci.*, *4*, 55–61, doi:10.1038/ngeo1036.

Liu, K., A. Levander, F. Niu, and M. S. Miller (2011), Imaging crustal and upper mantle structure beneath the Colorado Plateau using finite-frequency Rayleigh wave tomography, *Geochem. Geophys. Geosyst.*, *12*, Q07001, doi:10.1029/2011GC003611.

Liu, L., and M. Gurnis (2010), Dynamic subsidence and uplift of the Colorado Plateau, *Geology*, *38*(7), 663–666, doi:10.1130/G30624.1.

Lowry, A. R., and R. B. Smith (1995), Strength and rheology of the western U.S. Cordillera, *J. Geophys. Res.*, *100*(B9), 17,947–17,963, doi:10.1029/95JB00747.

Maceira, M., and C. J. Ammon (2009), Joint inversion of surface wave velocity and gravity observations and its application to central Asian basins shear velocity structure, *J. Geophys. Res.*, *114*, B02314, doi:10.1029/2007JB005157.

McQuarrie, N., and C. G. Chase (2000), Raising the Colorado Plateau, *Geology*, *28*(1), 91–94, doi:10.1130/0091-7613(2000)028<0091:RTCP>2.0.CO;2.

Moorkamp, M., A. G. Jones, and S. Fishwick (2010), Joint inversion of receiver functions, surface wave dispersion, and magnetotelluric data, *J. Geophys. Res.*, *115*, B04318, doi:10.1029/2009JB006369.

Morgan, P., and C. A. Swanberg (1985), On the Cenozoic uplift and tectonic stability of the Colorado Plateau, *J. Geodyn.*, *3*(1–2), 39–63.

Morgan, P., W. R. Seager, and M. P. Golombek (1986), Cenozoic thermal, mechanical and tectonic evolution of the Rio Grande rift, *J. Geophys. Res.*, *91*(B6), 6263–6276, doi:10.1029/JB091iB06p06263.

Moschetti, M. P., M. H. Ritzwoller, F. C. Lin, and Y. Yang (2010), Crustal shear wave velocity structure of the western United States inferred from ambient seismic noise and earthquake data, *J. Geophys. Res.*, *115*, B10306, doi:10.1029/2010JB007448.

Nagaya, M., H. Oda, H. Akazawa, and M. Ishise (2008), Receiver functions of seismic waves in layered anisotropic media: Application to the estimate of seismic anisotropy, *Bull. Seismol. Soc. Am.*, *98*(6), 2990–3006, doi:10.1785/0120080130.

Obrebski, M., R. A. Allen, F. Pollitz, and S. H. Hung (2011), Lithosphere-asthenosphere interaction beneath the western United States from the joint inversion of body-wave traveltimes and surface-wave phase velocities, *Geophys. J. Int.*, *185*, 1003–1021, doi:10.1111/j.1365-246X.2011.04990.x.

Okabe, M. (1979), Analytical expressions for gravity anomalies due to homogeneous polyhedral bodies and translations into magnetic anomalies, *Geophysics*, *44*(4), 730–741.

Owens, T. J., H. P. Crotwell, C. Groves, and P. Oliver-Paul (2004), SOD: Standing order for data, *Seismol. Res. Lett.*, *75*(4), 515–520, doi:10.1785/gssrl.75.4.515-a.

Parsons, T., J. McCarthy, W. M. Kohler, C. J. Ammon, H. M. Benz, J. A. Hole, and E. E. Criley (1996), Crustal structure of the Colorado Plateau, Arizona: application of new long-offset seismic data analysis techniques, *J. Geophys. Res.*, *101*(B5), 11,173–11,194, doi:10.1029/95JB03742.

Roy, M., J. K. MacCarthy, and J. Selverstone (2005), Upper mantle structure beneath the eastern Colorado Plateau and Rio Grande rift revealed by Bouguer gravity, seismic velocities, and xenolith data, *Geochem. Geophys. Geosyst.*, *6*, Q10007, doi:10.1029/2005GC001008.

Roy, M., T. H. Jordan, and J. L. Pederson (2009), Colorado plateau magmatism and uplift by warming of heterogeneous lithosphere, *Nature*, *459*(7249), 978–982, doi:10.1038/nature08052.

Sahagian, D., A. Proussevitch, and W. Carlson (2002), Timing of Colorado Plateau uplift: Initial constraints from vesicular basalt-derived paleoelevations, *Geology*, *30*(9), 807–810, doi:10.1130/0091-7613(2002)030<0807:TOCPUI>2.0.CO;2.

Savage, M. K., and A. F. Sheehan (2000), Seismic anisotropy and mantle flow from the Great Basin to the Great Plains, western United States, *J. Geophys. Res.*, *105*(B6), 13,715–13,734, doi:10.1029/2000JB900021.

Schmandt, B., and E. Humphreys (2010), Complex subduction and small-scale convection revealed by body-wave tomography of the western United States upper mantle, *Earth Planet. Sci. Lett.*, *297*(3–4), 435–445, doi:10.1016/j.epsl.2010.06.047.

Sigloch, K. (2011), Mantle provinces under North America from multi-frequency *P* wave tomography, *Geochem. Geophys. Geosyst.*, *12*, Q02W08, doi:10.1029/2010GC003421.

Sine, C. R., D. Wilson, W. Gao, S. P. Grand, R. Aster, J. Ni, and W. S. Baldridge (2008), Mantle structure beneath the western edge of the Colorado Plateau, *Geophys. Res. Lett.*, *35*, L10303, doi:10.1029/2008GL033391.

Snelson, C. M., T. J. Henstock, G. R. Keller, K. C. Miller, and A. Levander (1998), Crustal and uppermost mantle structure along the Deep Probe seismic profile, *Rocky Mt. Geol.*, *33*(2), 181–198, doi:10.2113/33.2.181.

Spence, W., and R. S. Gross (1990), A tomographic glimpse of the upper mantle source of magmas of the Jemez lineament, New Mexico, *J. Geophys. Res.*, *95*(B7), 10,829–10,849, doi:10.1029/JB095iB07p10829.

Spencer, J. E. (1996), Uplift of the Colorado Plateau due to lithosphere attenuation during Laramide low-angle subduction, *J. Geophys. Res.*, *101*(B6), 13,595–13,609, doi:10.1029/96JB00818.

Spencer, J. E., S. M. Richard, S. J. Reynolds, R. J. Miller, M. Shafiqullah, W. G. Gilbert, and M. J. Grubensky (1995), Spatial and temporal relationships between mid-Tertiary magmatism and extension in southwestern Arizona, *J. Geophys. Res.*, *100*(B6), 10,321–10,351, doi:10.1029/94JB02817.

Thompson, G. A., and M. L. Zoback (1979), Regional geophysics of the Colorado Plateau, *Tectonophysics*, *61*(1–3), 149–181, doi:10.1016/0040-1951(79)90296-8.

Tokam, A.-P. K., C. T. Tabod, A. A. Nyblade, J. Julià, D. A. Wiens, and M. E. Pasyanos (2010), Structure of the crust beneath Cameroon, West Africa, from the joint inversion of Rayleigh wave group velocities and receiver functions, *Geophys. J. Int.*, *183*(2), 1061–1076, doi:10.1111/j.1365-246X.2010.04776.x.

van Wijk, J. W., W. S. Baldridge, J. van Hunen, S. Goes, R. Aster, D. D. Coblentz, S. P. Grand, and J. Ni (2010), Small-scale convection at the edge of the Colorado Plateau: Implications for topography, magmatism, and evolution of Proterozoic lithosphere, *Geology*, *38*(7), 611–614, doi:10.1130/G31031.1.

Wessel, P., and W. H. F. Smith (1998), New, improved version of the Generic Mapping Tools released, *EOS Trans. AGU*, *79*(47), 579.

West, M., J. Ni, W. S. Baldridge, D. Wilson, R. Aster, W. Gao, and S. Grand (2004), Crust and upper mantle shear wave structure of the southwest United States: Implications for rifting and support for high elevation, *J. Geophys. Res.*, *109*, B03309, doi:10.1029/2003JB002575.

Wilson, D. C., R. Aster, S. Grand, J. Ni, and W. S. Baldridge (2010), High-resolution receiver function imaging reveals Colorado Plateau lithospheric architecture and mantle-supported topography, *Geophys. Res. Lett.*, *37*, L20313, doi:10.1029/2010GL044799.

Wolf, L. W., and J. J. Cipar (1993), Through thick and thin: A new model for the Colorado Plateau from seismic refraction data from Pacific to Arizona Crustal Experiment, *J. Geophys. Res.*, *98*(B11), 19,881–19,894, doi:10.1029/93JB02163.

Wolfe, J. A., C. E. Forest, and P. Molnar (1998), Paleobotanical evidence of Eocene and Oligocene paleoaltitudes in midlatitude western North America, *Geol. Soc. Am. Bull.*, *110*(5), 664–678, doi:10.1130/0016-7606(1998)110<0664:PEOEAO>2.3.CO;2.

Yang, Y., and D. Forsyth (2006), Regional tomographic inversion of the amplitude and phase of Rayleigh waves with 2-D sensitivity kernels, *Geophys. J. Int.*, *166*(3), 1148–1160, doi:10.1111/j.1365-246X.2006.02972.x.

Yoo, H. J., R. B. Herrmann, K. H. Cho, and K. Lee (2007), Imaging the three-dimensional crust of the Korean peninsular by joint inversion of surface-wave dispersion and teleseismic receiver functions, *Bull. Seismol. Soc. Am.*, *97*(3), 1002–1011, doi:10.1785/0120060134.

Zandt, G., S. Myers, and T. Wallace (1995), Crust and mantle structure across the Basin and Range–Colorado Plateau boundary at 37°N latitude and implications for Cenozoic extensional mechanism, *J. Geophys. Res.*, *100*(B6), 10,529–10,548, doi:10.1029/94JB03063.

I. W. Bailey and M. S. Miller, Department of Earth Sciences, University of Southern California, 3651 Trousdale Pkwy., ZHS 118, Los Angeles, CA 90034, USA.

A. Levander and K. Liu, Department of Earth Sciences, Rice University, 6100 Main St., PO Box 1892, MS 126, Houston, TX 77005, USA.